

Lab Report 1: Passive and Active Characteristics of Neurons

Ressa Reneth Sarreal

PHYS 4250/8814

January 12, 2022

Objectives: This lab is designed to create a neuron using the theory described in class and to measure passive characteristics and some simple dynamic behavior. Goals of this lab is to: 1. Build an electronic neuron 2. Study the time and space constants as a function of parameters in the circuit. 3. Quantify some simple dynamics of an active neuron.

Materials: Two breadboards, five $100\mu F$ capacitors, five $10k\Omega$ resistors, five $1k\Omega$ resistors, five $220\mu F$ capacitors, five 100Ω resistors, five 130Ω resistors, oscilloscope, four oscilloscope channel cables, 9 V battery, battery-wire adapter.

1.1 Construct two passive neurons

The following neuron cable model was constructed on a breadboard using the following resistor and capacitor values for five membrane segments.

Neuron 1: $c_m = 100\mu F$, $r_m = 10k\Omega$, $r_a = 1k\Omega$

Neuron 2: $c_m = 220\mu F$, $r_m = 100\Omega$, $r_a = 130\Omega$

A 9 V battery was used to supply external power to the neuron circuits. All output neuron circuit responses were observed through an oscilloscope.

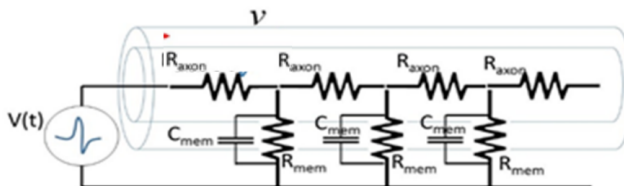


Figure 1.1: Neuron Cable Model, extracellular resistance is 0.

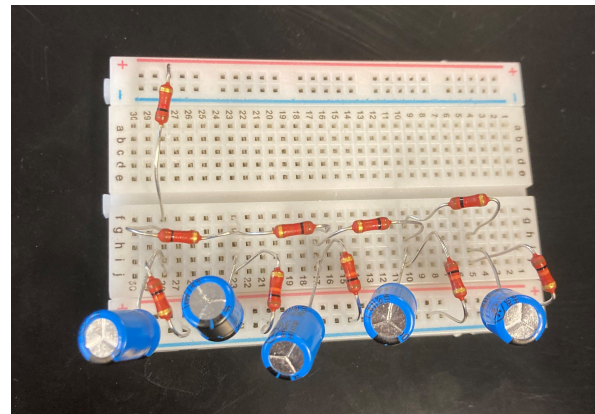


Figure 1.2: Neuron 1

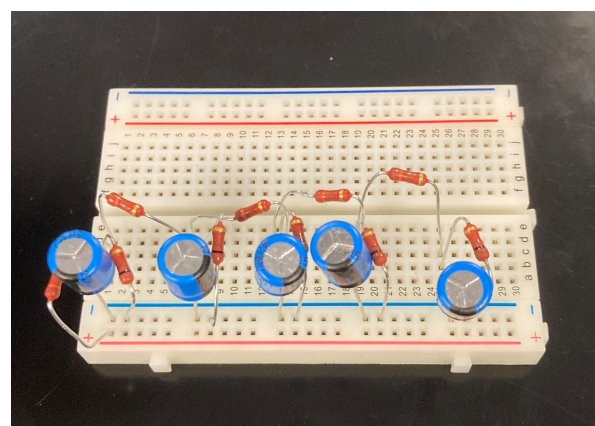


Figure 1.3: Neuron 2

1.2 Calculating neuron time constants

Q1: Report the actual values of c_m , r_m , and r_a that you used for your circuit(s) and measure the resistors with a multimeter to confirm. Measure the actual time constant on your oscilloscope and calculate what should it be from the theory of the circuit, report your experimental and theoretical values. If there are any differences between theory and experiments discuss where they could come from? Report these values for your second model neuron.

The measured r_m values ranged from 9.93 k Ω to 9.98 k Ω . The measured r_a values ranged from 999 Ω to 1007 Ω .

Capacitance values were not measured during this lab session.

Using the first neuron to solve for the time constant, τ , shown in 1.1

$$\tau = c_m r_m \quad (1.1)$$

The calculated time constant for one membrane segment is $\tau = 1\text{s}$.

Calculated below using the discharge response portion of the plot shown in Figure 1.4, the measured time constant was 1.08 s. Though the difference is only 0.08 s, this difference may have been caused by the tolerances allowed in the actual resistor and capacitor values.

$$V_{\text{inf}} = V_o e^{-\frac{t}{\tau}} \quad (1.2)$$

$$\tau = \frac{t}{\ln\left(\frac{V_o}{V_{\text{inf}}}\right)} \quad (1.3)$$

$$\tau = \frac{0.64}{\ln\left(\frac{9.32}{5.16}\right)} \quad (1.4)$$

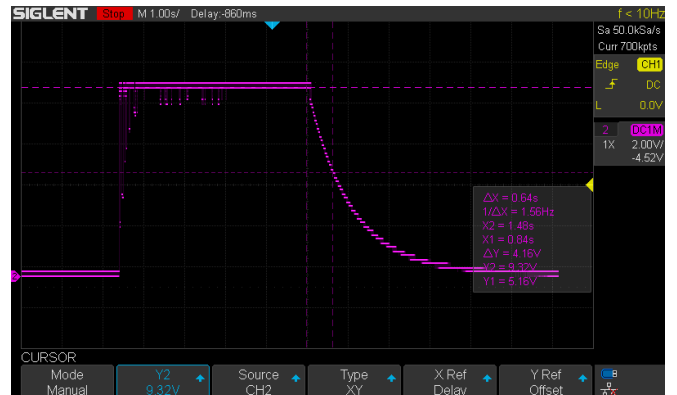


Figure 1.4: One membrane segment charge and discharge response plot.

Measurements were not able to be made for the second neuron (due to fire evacuation). The calculated time constant for the second neuron is $\tau = 0.022\text{s}$. With a smaller time constant, the expected rise and fall rates of the membrane voltage are greater than those shown in Figure 1.4.

1.3 Calculating neuron space constants

Q2. Plot the points as a function of distance from the power source (what are your units of distance?) and fit them with an exponential (either by hand or with a computer). What is the spatial time constant you obtain from experiments and theory? If there are differences explain what could cause it. Remember to do this for both neurons.

Using the first neuron to solve for the space constant, λ , shown in Equation 1.5. The calculated space constant for each segment is $\lambda = 3.16$ segments. Note that the units for r_m in this lab context are [$\Omega \cdot \text{segment}$] and the units for r_a are [$\frac{\Omega}{\text{segment}}$], making the units for the space constant, λ , membrane "segments".

$$\lambda = \sqrt{\frac{r_m}{r_a}} \quad (1.5)$$

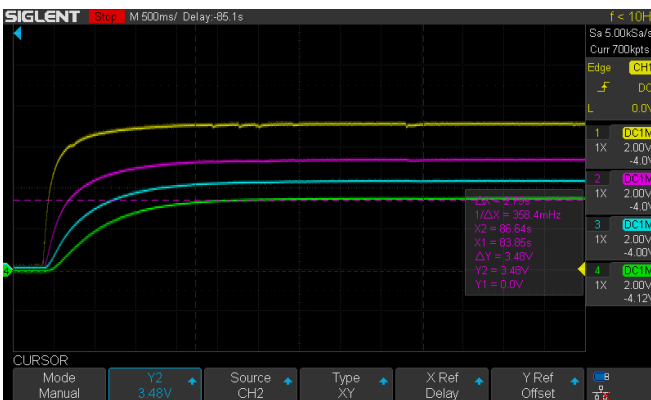


Figure 1.5: Four membrane segment charge and discharge response used to calculate the space constant. Yellow corresponds with the first segment, magenta corresponds with the second segment, blue corresponds with the third segment, and green corresponds with the fourth segment.

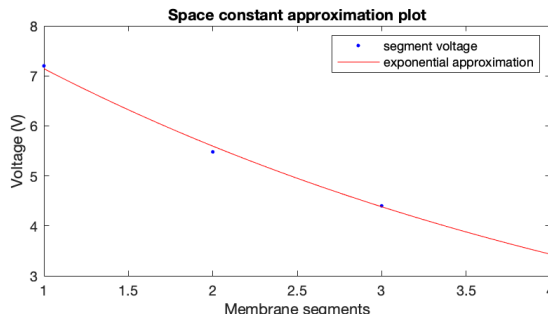


Figure 1.6: MATLAB plot of measured voltage measurements per membrane segment and the exponential curve approximation.

Using the peak voltage measurements from the oscilloscope, shown in Figure 1.5, an exponential curve was fitted to the data points. The approximated exponential function is $f(x) = 9.12e^{-\frac{x}{4.09}}$. Therefore, the space constant is $\lambda = 4.09$ segments. Differences may have been caused by the variance in the actual resistor and capacitor values.

The second neuron space constant was not measured (due to the fire evacuation).

1.4 The conduction velocity of neurons

Q4. Calculate the approximate speed of nerve impulses (λ/τ) using these two axon models, assuming passive transport.

From equations 1.1 and 1.5,

$$\frac{\lambda}{\tau} = \frac{1}{c_m} \sqrt{\frac{r_a}{r_m}} \quad (1.6)$$

Therefore, the approximate speed of a nerve impulse is 3162.2 segments per second.

Q5. Imagine you want to simulate a larger diameter neuron (Twice the diameter of your first neuron). Following the derivation in class, how should r_m , r_a and c_m change. Recall that the derivations in class are based assuming a uniform cylindrical cable. Assume that the membrane resistance arises from a uniform density of ion channels that is constant regardless of increasing size. Assume that the axon resistance arises from a uniform resistive fluid, which is the same as a uniformly conductive fluid.

The first assumption states that the membrane resistance is dependent on a uniform density and this density remains constant despite the neuron doubling in diameter; therefore, the membrane resistance remains the same per segment. The total capacitance of the axon will increase with the increase in diameter (causing the surface area of the "membrane capacitor" to double) by a factor of two. Similarly, the membrane capacitance per segment does not change. With the axon resistance, since the units for each segment is $\Omega/\text{segment}$, with the increase in diameter, since this resistance is dependent on the distance of propagation along the axon, the total resistance of the axon has increased by a factor of four (since the resistance depends on a radius-squared term) therefore, since the length of the axon has not changed, and total resistance increased by a factor of four, the axon resistance increased by a factor of four.

The solution above regarding the membrane resistance and capacitance is dependent on an additional assumption that the distance of measurements (membrane thickness) is constant.

1.5 Investigate the effect of a quick stimulus (impulse) on your neurons

Consider a function $G(x, t)$ that satisfies this differential equation for an external current i_{ext} that is ap-

plied almost instantaneously in time and one place in space.

$$i_m = c_m \frac{dV_m}{dt} + \frac{V_m}{r_m} + i_{ext} \quad (1.7)$$

$$\frac{\partial}{\partial t} G(x, t) - \frac{\partial^2}{\partial x^2} G(x, t) + G(x, t) = \delta(t)\delta(x) \quad (1.8)$$

Q7a(for graduate students). Show that using a Fourier transform in space this equation can be transformed into a single first order ordinary differential equation only in time.

$$\int_{-\infty}^{+\infty} \left(\frac{\partial}{\partial t} G(x, t) - \frac{\partial^2}{\partial x^2} G(x, t) + G(x, t) \right) e^{-j k x} dx \quad (1.9)$$

After taking the Fourier transforms of each of the terms of the partial differential equation, the following are obtained:

$$\mathcal{F}\left(\frac{\partial G}{\partial x}\right) = jk \mathcal{F}(G) \quad (1.10)$$

$$\mathcal{F}\left(\frac{\partial^2 G}{\partial x^2}\right) = -k^2 \mathcal{F}(G) \quad (1.11)$$

$$\mathcal{F}\left(\frac{\partial G}{\partial t}\right) = \frac{\partial}{\partial t} \mathcal{F}(G) \quad (1.12)$$

$$\mathcal{F}(\delta(t)\delta(x)) = \delta(t) \quad (1.13)$$

$$\frac{\partial}{\partial t} \mathcal{F}(G) + k^2 \mathcal{F}(G) + \mathcal{F}(G) = \delta(t) \quad (1.14)$$

Therefore, from equation 1.14, after taking a Fourier transform in the spatial domain, the result is a first-order differential equation in time.

Q7b(for graduate students). Show that this equation can be integrated and the solution $G(k, t)$ can be written in terms of an exponential and a heaviside step function $\Theta(t)$.

Solving the ordinary differential equation shown in equation 1.14 defined as the following where $y = \mathcal{F}(G)$, $P(t) = (k^2 + 1)$, and $Q(t) = \delta(t)$

$$y' + P(t)y = Q(t) \quad (1.15)$$

The following equation is obtained, after establishing boundary conditions: x approaches positive and negative infinity, $G(x, 0)$ approaches 0, and $G(x, t) = 0$ when $t < 0$.

$$\mathcal{F}(G(x, t)) = \Theta(t) \mathcal{F}(G(k, 0)) e^{-(k^2+1)t} \quad (1.16)$$

$\mathcal{F}(G(k, 0))$ is the spatial response of the Green's function when $t = 0$, representing some boundary conditions. Let $f(k) = \mathcal{F}(G(k, 0))$.

$$G(k, t) = \mathcal{F}(G(x, t)) = \Theta(t) \mathcal{F}(f(k)) e^{-(k^2+1)t} \quad (1.17)$$

Therefore, $G(k, t)$ can be written in terms of an exponential and a heaviside step function.

Q7c(for graduates). Then by taking an inverse Fourier transform of the Green's function $G(k, t)$, show that one will obtain the following solution:

$$G(x, t) = \frac{\Theta(t)}{2\sqrt{\pi t}} e^{-(t+\frac{x^2}{4t})} \quad (1.18)$$

Taking the inverse Fourier transform of equation 1.17,

$$G(x, t) = \frac{\Theta(t)}{2\pi} \int_{-\infty}^{+\infty} \left(\mathcal{F}(f(k)) e^{-(k^2+1)t} \right) e^{-j k x} dx \quad (1.19)$$

$$G(x, t) = \frac{\Theta(t)}{2\pi} \int_{-\infty}^{+\infty} \left(\int_{-\infty}^{+\infty} (f(y) e^{-iky}) e^{-j k x} dy \right) ... \\ ... e^{-j k x} dx \quad (1.20)$$

$$G(x, t) = \Theta(t) \int_{-\infty}^{+\infty} \left(\frac{1}{2\pi} \int_{-\infty}^{+\infty} (e^{ik(x-y)-(k^2+1)t}) dk \right) ... \\ ... f(y) dy \quad (1.21)$$

Let $\xi = x - y$. Then the inner Fourier transform in equation 1.21 can be established as the

inverse Fourier transform of a Gaussian function:
 $\mathcal{F}^{-1}(e^{-(k^2+1)t})$.

$$G(x, t) = \Theta(t) \int_{-\infty}^{+\infty} \left(\frac{1}{2\pi} \int_{-\infty}^{+\infty} (e^{ik\xi} e^{-(k^2+1)t}) dk \right) ... f(y) dy \quad (1.22)$$

The inverse Fourier transform of the Gaussian function is

$$\mathcal{F}^{-1}(e^{-(k^2+1)t}) = \frac{e^{-\frac{\xi^2}{4t}}}{2\sqrt{\pi t}} \quad (1.23)$$

therefore,

$$G(x, t) = \Theta(t) \int_{-\infty}^{+\infty} \frac{e^{-(t+\frac{\xi^2}{4t})}}{2\sqrt{\pi t}} f(y) dy \quad (1.24)$$

Substituting $\xi = x - y$ a convolution integral is obtained. Also, since $f(y)$ represents the initial function, an impulse response, the convolution can be solved as the following:

$$G(x, t) = \Theta(t) \int_{-\infty}^{+\infty} \frac{e^{-(t+\frac{(x-y)^2}{4t})}}{2\sqrt{\pi t}} \delta(y) dy \quad (1.25)$$

Therefore,

$$G(x, t) = \frac{\Theta(t)}{2\sqrt{\pi t}} e^{-(t+\frac{x^2}{4t})} \quad (1.26)$$

Q8. Show that this is indeed a solution of the general equation above (by plugging it into the PDE equation above).

Substituting $G(x, t)$ into the PDE shown in equation 1.8,

$$\begin{aligned} \frac{\partial}{\partial t} \left(\frac{\Theta(t)}{2\sqrt{\pi t}} e^{-(t+\frac{x^2}{4t})} \right) - \frac{\partial^2}{\partial x^2} \left(\frac{\Theta(t)}{2\sqrt{\pi t}} e^{-(t+\frac{x^2}{4t})} \right) + \\ \left(\frac{\Theta(t)}{2\sqrt{\pi t}} e^{-(t+\frac{x^2}{4t})} \right) = \delta(t)\delta(x) \end{aligned} \quad (1.27)$$

and after performing the partial derivations, the following equation is obtained

$$\begin{aligned} [[\delta(t)t^{-1/2} - \frac{\Theta(t)}{2}t^{-1/2} - \Theta(t)t^{-1/2} + \frac{x^2}{4}t^{-3/2}\Theta(t)] \\ + [\frac{\Theta(t)}{2}t^{-3/2} - \frac{x^2}{4}t^{-3/2}\Theta(t)] + \\ [\Theta(t)t^{-1/2}]] \frac{e^{-(t+\frac{x^2}{4t})}}{2\sqrt{\pi}} \end{aligned} \quad (1.28)$$

and terms can be cancelled with each other, leaving

$$\delta(t) \frac{e^{-(t+\frac{x^2}{4t})}}{2\sqrt{\pi t}} \quad (1.29)$$

The final step is understanding that

$$\lim_{x \rightarrow 0^+} \frac{e^{-(t+\frac{x^2}{4t})}}{2\sqrt{\pi t}} = \delta(x) \quad (1.30)$$

Therefore, and the PDE is equivalent on both sides after substituting the provided Green's function, equation 1.18.

Q9a. Now apply an impulse of current to the start of your model neuron and record the resulting v vs. t plot at node 4 or 5 on your oscilloscope. Write down the shape, magnitude, rising and falling times of the response.

Shown in green in Figure 1.7, the fourth node exhibits a small, asymmetrical bump (rise time is shorter than the fall time). The peak magnitude of the response is 1 V, rise time is 564 ms, and fall time is 0.98 s.

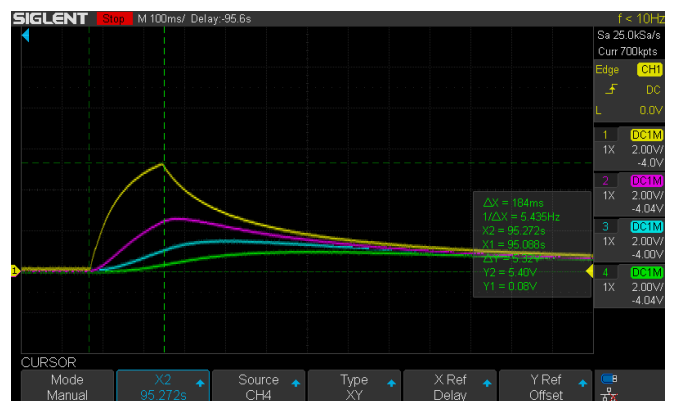


Figure 1.7: Four membrane segment charge and discharge response to an impulse. Yellow corresponds with the first segment, magenta corresponds with the second segment, blue corresponds with the third segment, and green corresponds with the fourth segment.

Q9b. Plot the $G(x, t)$ function above of at a point in space comparable to where you recorded in your model neuron. Report the shape, magnitude, rising and falling times of this equation to your recorded values.

Shown in green in Figure 1.8, the fourth node exhibits a small, asymmetrical bump (rise time is shorter than the fall time). The peak magnitude of the response is 0.0406 V, rise time is 780 ms, and fall time is 1.095 s.

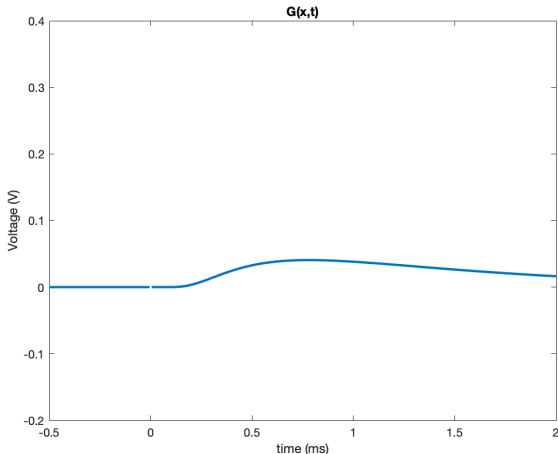


Figure 1.8: The Green's function $G(x, t)$, where $x = 2$ to emulate the fourth node curve from Figure 1.7.

Q9c. Do they match qualitatively?

The green curve from Figure 1.7 and the curve in Figure 1.8 qualitatively look very similar in shape (a small bump). Specifically the rise rate is greater than the fall rate, giving the curve an asymmetric quality.

Q9d. Do they match quantitatively? To do this comparison, we need to have x and t on the same scale.

Rescale time in your $G(t)$ plot such that the rise time matches the $V(t)$ plot. After the rescaling are the falling times the same? (hint: this can also be done by comparing the ratio of the two rise times to the ratio of the two falling times.

From the experimental data, the rise-to-fall ratio of the curve is approximately 37:63. From the obtained Green's function, the ratio is approximately 41:59. Quantitatively, the curves have very similar rise and fall times (rise times only exhibit a 5% error).

Q9e. Provide at least three assumptions that go into the equation above that might be violated in your model neuron? Which of these is most likely to explain the difference and why?

Three assumptions that were made when solving the equation above that may be violated by the neuron model are the following:

1. The space variable, x , was assigned the value of 2 in the Green's function and there is no direct comparison to the space variable from the experimental setup (lambda and tau are not represented in the Green's function PDE).
2. The inputted impulse resembled an exact dirac delta function.
3. The Green's function in general assumes a linear differential operator is used on the input and this may not have been exactly true for this experimental neuron circuit model (inductance, parasitic capacitance).

The most likely assumption that caused the difference between the green curve in Figure 1.7 and the curve in Figure 1.8 is the first one due to the inaccurate representation of the spatial measurement. Though this assumption probably caused significant differences, the second assumption (impulse input) also plays a very large role in the outcome of the experimental data.

Sippin' TEA with Crayfish

Lynn Jin
Zach Mobille
Ressa Reneth Sarreal
Biswadeep Chakraborty

January 31, 2022

Abstract

We explore how the extracellular potential waveform of a crayfish nerve is modulated by the potassium channel blocker Tetraethylammonium (TEA). In particular, the action potential duration and amplitude are quantified with respect to TEA concentration. Our findings are supported by previous studies that investigate the effects of potassium blockers on crayfish neurons.

Introduction

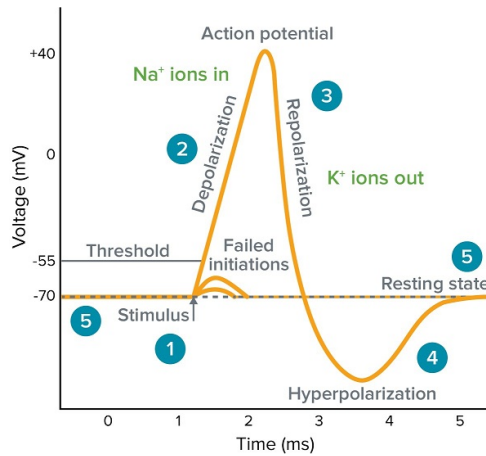
- ▶ Crayfish have hundreds of neurons along the ventral nerve cord (VNC)
- ▶ Membrane potential can be measured intracellularly as well as extracellularly
- ▶ The membrane potential (over space and time) is affected by intracellular to extracellular ion ratios, membrane resistance, membrane capacitance as well as axon resistance



Extracellular VNC measurement setup for a crayfish

Introduction (continued)

- ▶ An action potential is the response of a neuron after a certain membrane voltage threshold is reached (spikes in membrane voltage)
- ▶ TEA is a K^+ blocker that will inhibit activity across K^+ membrane channels
- ▶ Neurons have different responses depending on their function
- ▶ **How may we use ion blockers to modify neuron responses?**



General action potential stages (photo credit: moleculardevices.com)

Hypothesis

Prediction: In an intracellular recording, the entire waveform is scaled down in the vertical direction. The action potential duration increases. In an extracellular recording, this would correspond to a lengthened duration and smaller magnitude responses.

1. Amplitude reduction from $E_j = \frac{RT}{Z_j F} \ln \left(\frac{[X_o]_j}{[X_i]_j} \right)$
2. Introducing K⁺ blocker will increase membrane resistance because the K⁺ channel conductance, g_K , decreases.
 - ▶ $\tau = r_m c_m$; increase r_m leads to increase in time constant
3. $Vm_{rest} = \frac{\sum_j g_j E_j}{\sum_j g_j}$; possible shift in resting potential

Methodology - Crayfish Dissection and probing

1. Prepare the crayfish for dissection by burying it in ice to force it into an unconscious state
2. Separate the tail from the body then clip off swimmerets
3. Pin the tail in a petri dish and fill with saline solution
4. Slightly to the side of the blueish center line along the crayfish (to avoid cutting the VNC), make an incision.
5. Create incisions to the left and right at the top of the first incision to create access flaps to the VNC
6. Connect the electrode to the VNC using pipette suction, place the ground wire in the saline solution and observe extracellular readings through the oscilloscope

Methodology - Perfusion

1. Obtain two, high-volume pipettes
2. Use one pipette to remove the present solution while another pipette is used to introduce the new solution until the pipette is empty. Make sure the rate of solution removal and replacement is similar (or the same if possible).
3. Repeat the step 2 to completely replace the previous solution

Methodology - Preprocessing and Measurements

Pre-Processing:

1. Identify cutoff frequency from Power Spectrum Density
2. Apply low-pass filter
 - 2.1 We use a 2nd order Butterworth filter

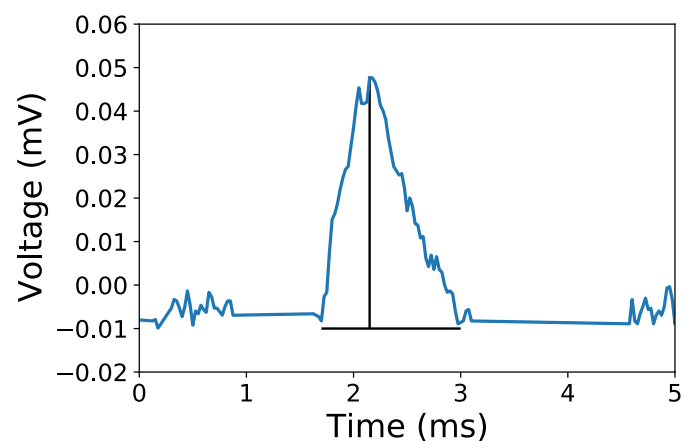
Measuring Shift

1. Plotted Histogram for the filtered data
2. Measure the mean of the data from the histogram to compare the shift of signal

Methodology- Measurements

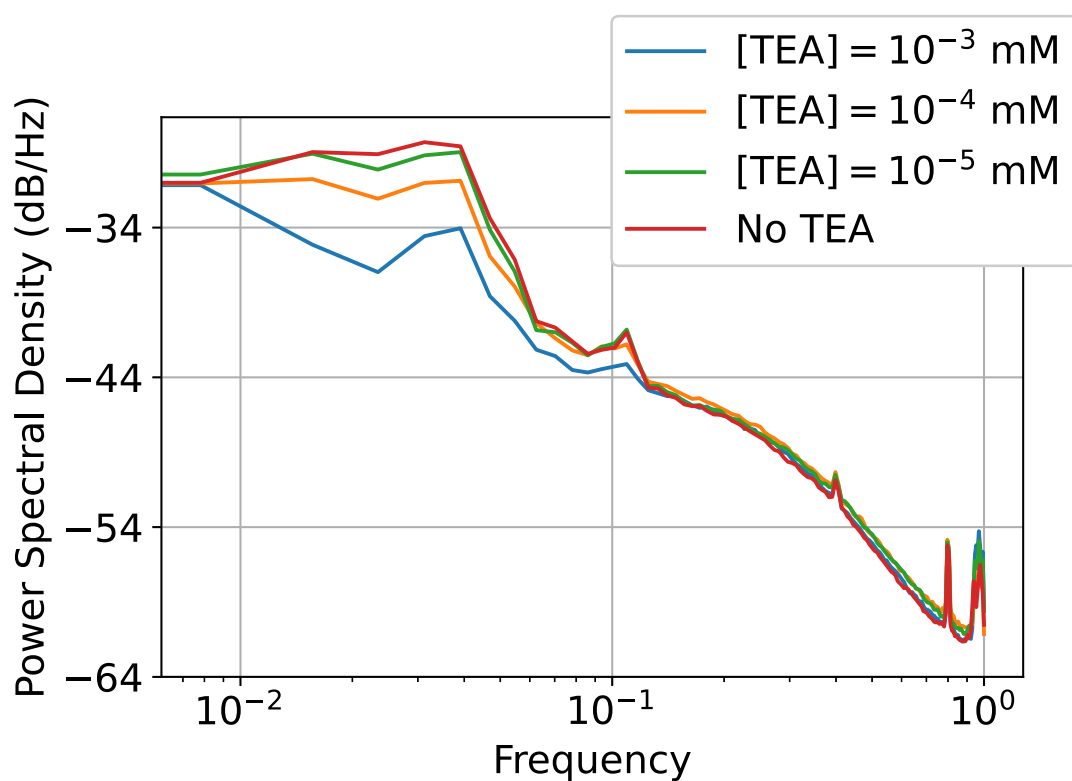
Measuring Spike Width and Amplitude:

1. Measure the peaks of the data to get the amplitudes and spike width
2. We take -0.01 as the baseline cutoff to measure the voltage amplitude and width



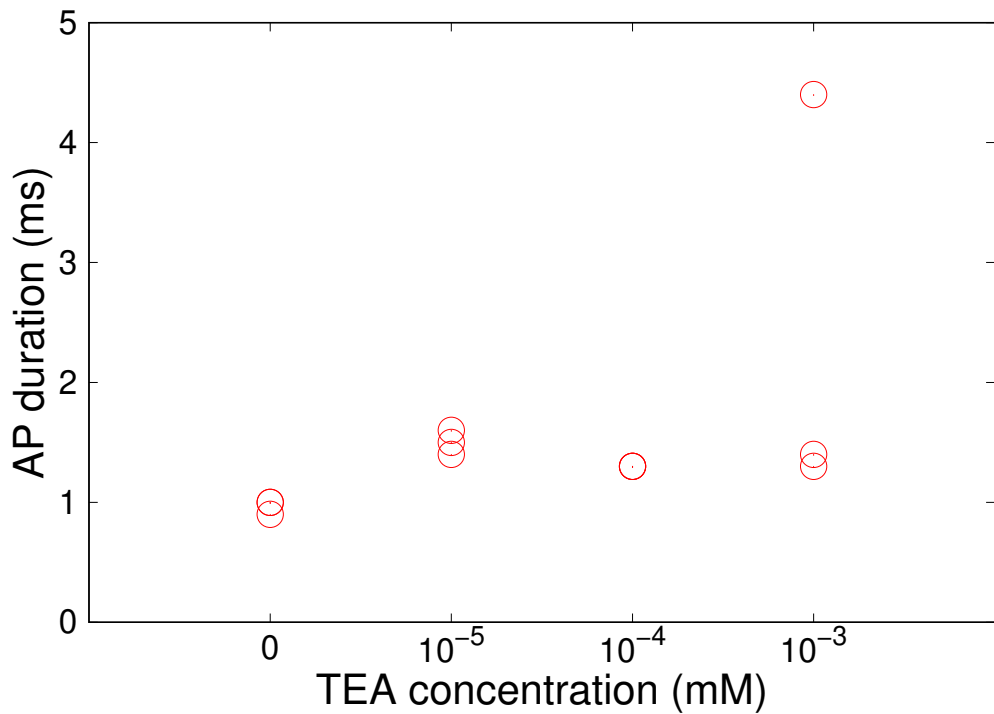
Motivation

Power Spectral Density shows the variation of power for low-frequency signals with different TEA concentrations:



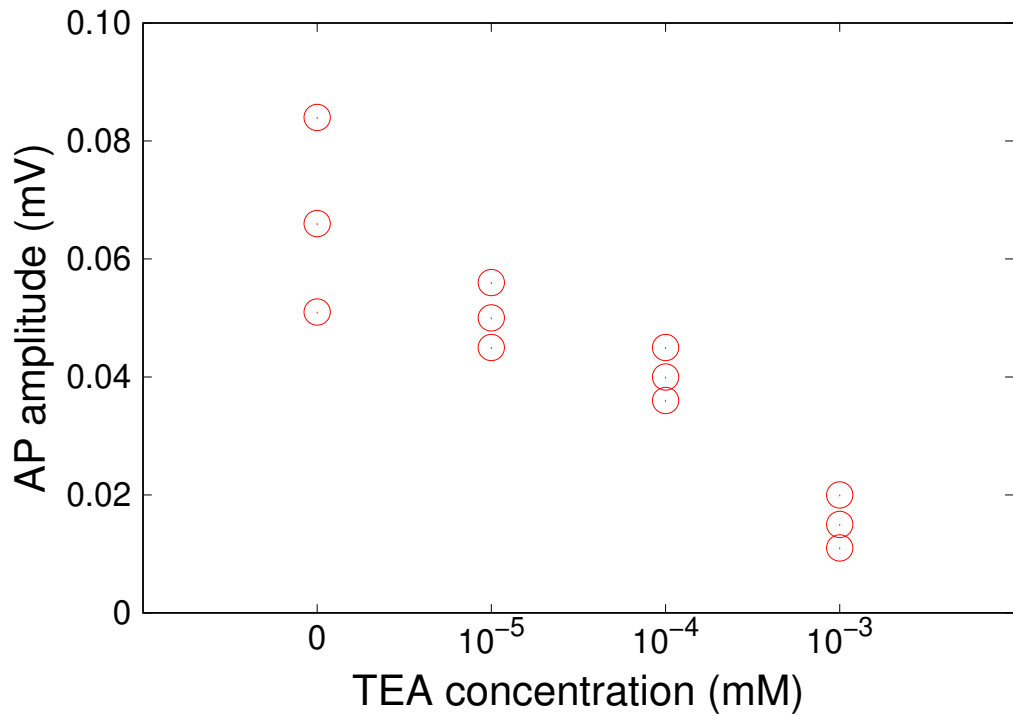
Results

Average action potential (AP) duration at $[TEA]=0$ mM is lower than that at $[TEA]=10^{-3}$ mM.



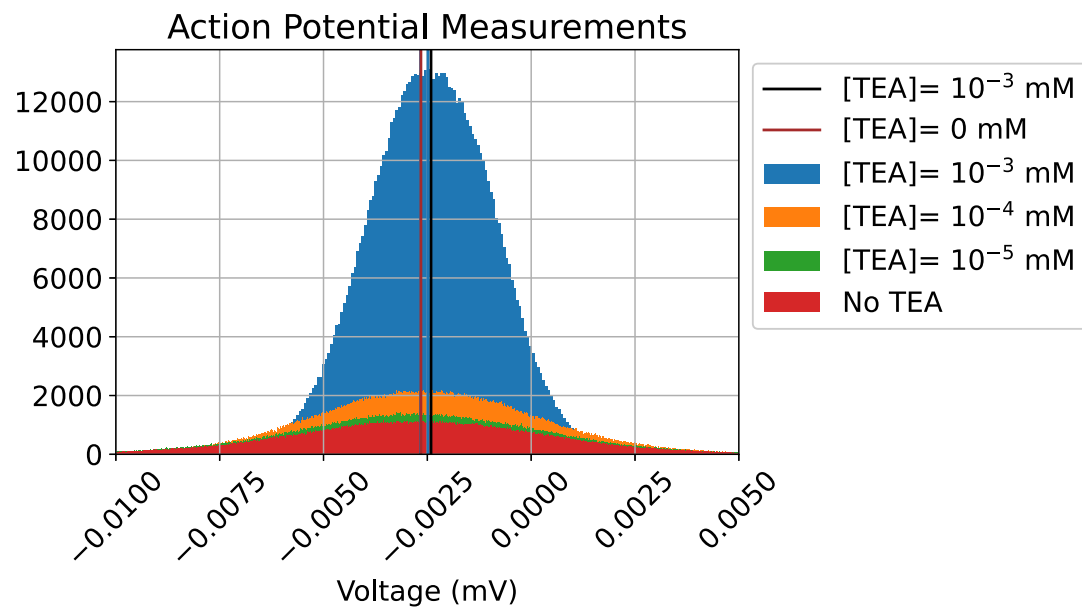
Results

Amplitude of extracellular action potentials decays as more K⁺ blocker is perfused.



Results

Histogram showing the upward shift of spike means on addition of TEA



Discussion

- ▶ Our hypothesis supported by previous research regarding the effects of K^+ blockers on crayfish neuron responses [1, 2]
- ▶ Extracellular measurements may not correspond perfectly to our predictions made for intracellular membrane potential.

Conclusion

- ▶ Introduction of any concentration of TEA to the saline solution caused a slight increase in the action potential time and space constant. This increase did not vary with TEA concentration
- ▶ With an increase in TEA concentration, there was a decrease in action potential magnitude

References



Jen-Wei Lin.

Spatial variation in membrane excitability modulated by 4-ap-sensitive K^+ channels in the axons of the crayfish neuromuscular junction.

Journal of neurophysiology, 107(10):2692–2702, 2012.



Shobhana Sivaramakrishnan, George D Bittner, and Malcolm S Brodwick.

Calcium-activated potassium conductance in presynaptic terminals at the crayfish neuromuscular junction.

The Journal of general physiology, 98(6):1161–1179, 1991.

Thank you!

Questions?



Lab Report 2 Effects of Temperature on Transmembrane Voltage in Zebra Fish Cardiac Tissue

Ressa Reneth Sarreal, Biswadeep Chakraborty, Lynn Jin, Zachary Mobille

PHYS 4250/8814

February 9, 2022

Abstract- We explore how the transmembrane action potential response of a zebra fish heart ventricle is modulated by a change in temperature. In particular, the restitution curve action potential durations and bifurcations point are quantified with respect to three temperatures: 10 °C, 22 °C, and 25 °C. Our findings are supported by previous studies that investigate the effects of temperature on action potential duration and were supported by experimental results.

1.1 Introduction

The primary goal for the experiment depicted in this document is to observe the effects of temperature on the shape of an action potential. Specifically, an objective was to observe how action potential duration (APD) changes with a change in temperature; additionally, if the bifurcation point will shift on the restitution plot.

Our group hypothesized that with an increase in temperature, the action potential duration will increase. From class lectures, there were few equations that related temperature to the shape of an action potential. The only equation that related temperature to action potentials was the Nernst Potential equation, shown in equation 1.1, where R is the gas constant, T is temperature, Z is the charge of the ion, and F is the Faraday constant. This equation describes the equilibrium potential where each ion channel has no current flowing through. Though, some insight can be obtained through this equation with regard to the magnitude at which the action

potential will switch between depolarization and repolarization or hyperpolarization. For example, depolarization transitions to repolarization when the membrane potential reaches the Nernst potential of the sodium ion channel. The increase in temperature would indicate that the peak of the action potential and the downswing of the action potential would both be greater in magnitude, lightly implying it would take a longer time to complete the action potential; however, no firm predictions were made using this equation.

$$E_j = \frac{RT}{ZF} \ln \left(\frac{[X_o]_j}{[X_i]_j} \right) \quad (1.1)$$

Our prediction was made on the basis that there exists modifications to the Hodgkin-Huxley model equations that incorporate a scaling factor that depends on temperature [1]. Ementrout et. al equation 1.43 shows that dn/dt , dm/dt , and dh/dt are scaled by ϕ where Q_{10} is a scaling term dependent

the ratio of rates for an increase of temperature by $10 \text{ }^{\circ}\text{C}$, T is temperature, and T_{base} is a reference temperature. ϕ is defined below:

$$\phi = Q_{10}^{(T-T_{base})/10} \quad (1.2)$$

Therefore, with an increase in temperature, dn/dt , dm/dt , and dh/dt will also increase, creating shorter APDs.

Also, the bifurcation point will shift to a higher diastolic interval (to the right on the restitution curve). With a similar issue to the previously described prediction, another article was used to justify the prediction. Hodgkin and Huxley performed temperature experiments using the giant axon of a squid, having plotted the action potentials with varying temperatures side-by-side [2], the APDs had shortened, shown in Figure 1.1 which was pulled from their article, adding support to the previous prediction, and the diastolic intervals (DI) are presumed to vary less than the APDs. This secondary hypothesis is thus supported by this article.

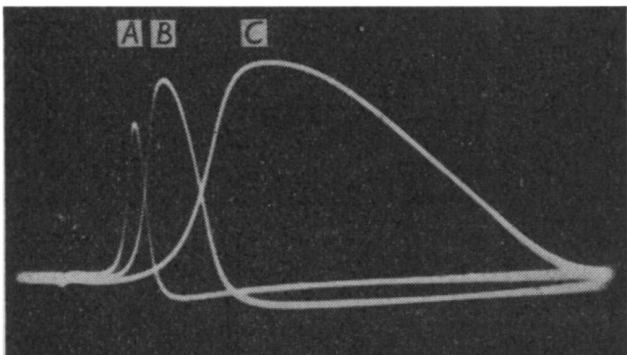


Figure 1.1: Records of action potentials at three temperatures, superimposed on the same base-line and stimulus artifact. Temperatures and amplitudes, respectively: A, 32.50 C., 74.5 mV; B, 38.5 0., 99 mV; C, 50C. 108-5mV. Time marks: 1msec [2].

1.2 Methodology

During this work, a dissected zebra fish heart was used and transmembrane signals were measured at the ventricle. Very fine pins were used to pin the fish heart to the petri dish and larger, conductive insect pins were inserted to opposite sides of the ventricle to induce an electric field across the ventricle instead of directly injecting current through the ventricle. Direct injection was not an option as the larger insect pins would severely damage the heart. For the experiment, the heart was submerged in low-calcium Tyrode solution of varying temperatures: 10 °C, 22 °C (room temperature), and 25 °C. These colder and hotter temperatures were achieved using an ice bucket and a hot plate respectively.

After the perfusion of each temperature of Tyrode solution, a stimulus is applied to the ventricle and observed through the oscilloscope after amplification with a gain of 1000. This signal is passed through an ADC and recorded using MATLAB. For each stimulus period, the action potential duration (APD) at 75% of the repolarization stage was recorded and the DI was recorded.

1.3 Results

The results at each of the temperatures will be discussed separately then discussed together at the end of this section.

1.3.1 Cold Temperature

The average APD and DI at 10 °C, between all stimulation periods, is 0.283 s and 0.4193 respectively. The obtained restitution curve is shown in Figure 1.2.

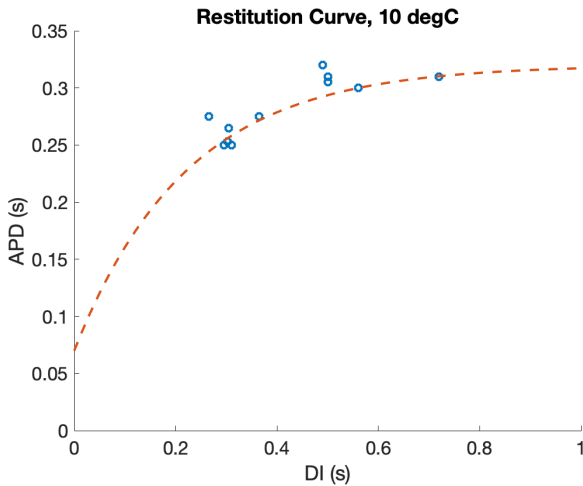


Figure 1.2: Restitution curve for transmembrane zebra fish ventricle recordings with a 10 °C Tyrode solution. The dashed red line is the fitted function $0.32 - 0.25e^{-4.5x} + 0.32$.

1.3.2 Room Temperature

The average APD and DI at 22 °C, between all stimulation periods, is 0.2466 s and 0.3681 respectively. The obtained restitution curve is shown in Figure 1.3.

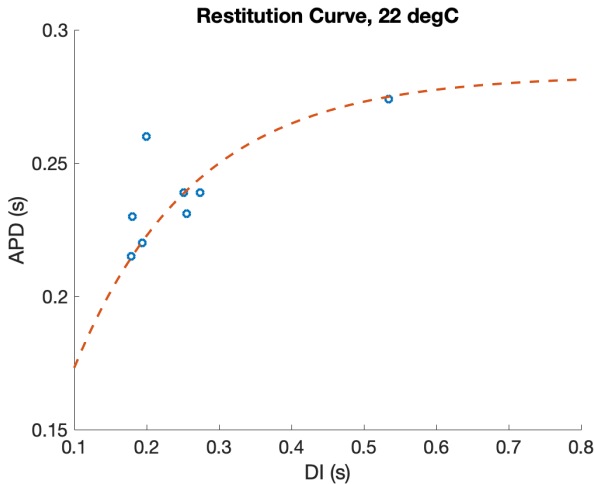


Figure 1.3: Restitution curve for transmembrane zebra fish ventricle recordings with a 22 °C Tyrode solution. The dashed red line is the fitted function $0.283 - 0.2e^{-6x}$.

1.3.3 Warm Temperature

The average APD and DI at 25 °C, between all stimulation periods, is 0.14174 s and 0.306 s respectively. The obtained restitution curve is shown in Figure 1.4.

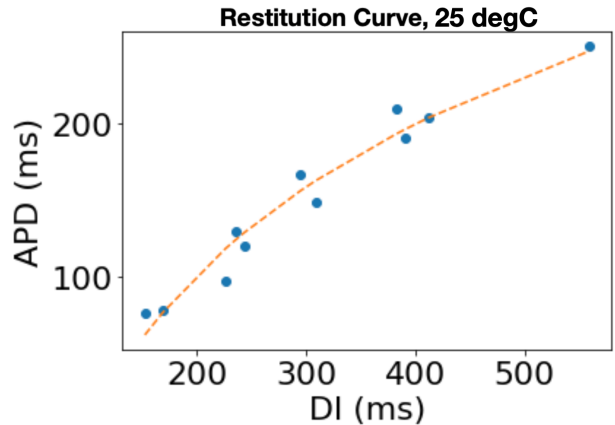


Figure 1.4: Restitution curve for transmembrane zebra fish ventricle recordings with a 22 °C Tyrode solution. The dashed orange line is the fitted function $-282.15 + 141.74\log(0.074x)$.

1.3.4 Temperature Comparison

Box plots were created to observe a general trend between temperatures. The box plot for DIs at varying temperatures is shown in Figure 1.5, and the box plot for APDs at varying temperatures is shown in Figure 1.6.

With increasing temperature, the average DI for each temperature did not exhibit any trend, but the DI did vary between temperatures. However, a downward trend was observed for APD with an increase in temperature. At 10 °C, the average APD is 0.283 s, and at 22 °C the APD decreases by 36.4 ms, and at 25 °C the APD decreased by an additional 104.86 ms.

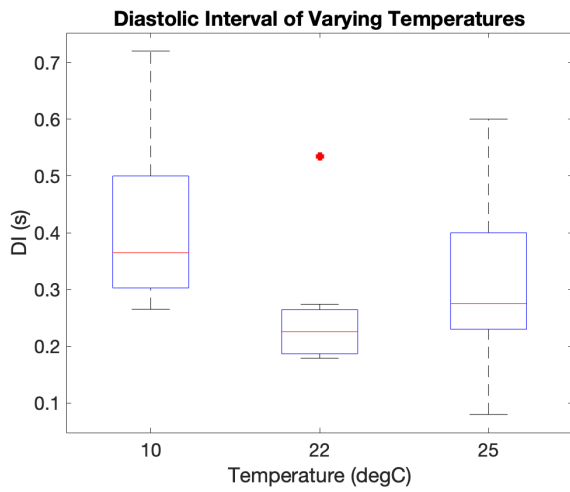


Figure 1.5: Box plot of the DIs at varying temperatures.

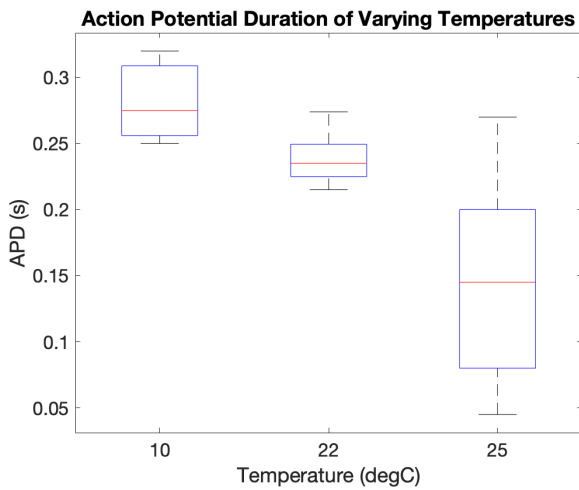


Figure 1.6: Box plot of the APDs at varying temperatures.

1.4 Discussion

First addressing strong conclusions made during the experiment, there is a distinct trend of decreasing APDs with increase in Tyrode solution temperature. Additionally, there are only few points of overlap of APDs between the selected temperatures, shown in Figure 1.6, which firmly supports the original hypothesis. The data supports the modified Hodgkin-

Huxley model which are reiterated in equations 1.3 through 1.5 below, where ϕ is defined in equation 1.2.

$$\frac{dn}{dt} = \phi[\alpha_n(V)(1-n) - \beta_n(V)n] \quad (1.3)$$

$$\frac{dm}{dt} = \phi[\alpha_m(V)(1-m) - \beta_m(V)m] \quad (1.4)$$

$$\frac{dh}{dt} = \phi[\alpha_h(V)(1-h) - \beta_h(V)h] \quad (1.5)$$

Some factors that may have led to differences between the literature and the results obtained in this experiment are that the action potentials of a giant axon of a squid and the action potentials of the ventricle of a zebra fish heart are very different. A more drastic change of APD was expected between the 10 °C and 22 °C Tyrode, referring to Figure 1.1; however, it is possible the calcium ion channels that are more prevalent in the heart model may have affected this relationship. Additionally the large difference between the 22 °C and 25 °C data may have been caused by the lapsed time between when the experiments were conducted. Some connection issues between the electrode and the ventricle were experienced between the two experiments.

Speaking more on the zebra fish ventricle action potentials– the zebra fish heart, the alternative being a frog heart, was originally selected to more easily observe bifurcation. Unfortunately, bifurcation was not easily spotted in this data set, but alternans were present for these temperatures. Additionally, exponential curve fitting to the restitution curves were

challenging with the obtained data set, especially for the 25 °C subset where a logarithmic function was fitted to the data points.

Though the experiment supported the overarching hypothesis that the APDs would decrease with an increase in temperature, the secondary hypothesis regarding the shift in bifurcation to a higher DI point on the restitution plot was neither proved nor disproved. An original concern was how the DI would vary with temperature as well. The data on DI for this experiment was inconclusive, so further assumptions on how the bifurcation point was affected cannot be made. The secondary hypothesis was neither proved nor disproved since the bifurcation point could not be identified in the data plots and this inference could not be made.

Key points of improvement if another iteration of

the experiment were to be performed in the future would be to obtain more data points to not only create a clearer restitution plot with a distinct bifurcation point, but to also analyze behavior of the DI with change in temperature.

1.5 Conclusion

Ultimately, our hypothesis regarding the increase in APD with increase in temperature was supported by the results of this experiment. However, the shift in bifurcation point could not be observed since the obtained plots did not exhibit a clear moment of bifurcation.

Adjustments to the experiment would include more consistent stimulation periods between each temperature as well as performing trials at more periods to create a cleaner restitution plot.

References

- [1] G. B. Ermentrout and D. H. Terman. Mathematical foundations of neuroscience. *Interdisciplinary Applied Mathematics*, 35, 2010.
- [2] A. L. Hodgkin and B. Katz. The effect of temperature on the action potential of the giant axon of the squid. *J. Physiol.*, 109, 1949.

Lab Report 3: Optical mapping of the effects of Octopamine and Cromakalim on frog heart cardiac activity

Ressa Reneth Sarreal, Biswadeep Chakraborty, Lynn Jin, Zachary Mobile

PHYS 4250/8814

March 4, 2022

Abstract- We explore how to observe action potential response in a frog heart using voltage-sensitive dye. The heart is exposed to three different solutions: low-calcium Tyrode, Octopamine, and Cromakalim. In particular, using restitution curves, action potential durations and diastolic intervals are quantified. Our findings are partially supported by previous studies that investigate the effects of the listed solutions on action potential duration and were supported by experimental results. The effects of Octopamine on a frog heart include an increase in action potential duration, and it was shown that the effects of Cromakalim include an increase in action potential firing rate.

3.1 Introduction

The primary goal for the experiment depicted in this document is to observe the effects of various drugs on the action potentials generated from a frog heart. Specifically, an objective was to observe how action potential duration (APD) changes when the heart is exposed to Octopamine and Cromakalim.

Based on findings from a literature review of the two drugs of interest, described in the following subsections, our group hypothesized that when the heart is exposed to Octopamine the observed action potentials will increase in duration and action potential peak amplitude will also increase. We predict that Cromakalim will cause shorter APDs which would also increase the frequency of firing action potentials. Reasoning behind these two hypotheses are explained in the following subsections which contain a brief literature review of the two drugs.

3.1.1 Octopamine

The exact effects of Octopamine on vertebrates is currently unknown; however Octopamine is structurally similar to noradrenaline [1]. Noradrenaline, also known as norepinephrine, increases the rate of uptake of Calcium and force of contraction of the heart [2, 3]. These effects are caused by an increase in extracellular calcium ion concentration [4]. Additionally, studies by Yamagishi have supported that Octopamine increases the frequency and amplitude of fired action potentials in a cardiac model [5].

An increase in extracellular calcium ion concentration affects the Nernst potential for the calcium ion channels per equation (3.1). This increase is the cause of the uptake of calcium, which increases the APD.

$$E_j = \frac{RT}{ZF} \ln \left(\frac{[X_o]_j}{[X_i]_j} \right) \quad (3.1)$$

3.1.2 Cromakalim

Cromakalim enables potassium ion channels to open more easily. Furthermore, a study was performed where it is shown that cardiac action potential duration was shortened and the contraction force was decreased. [6].

With potassium channels that open more easily, the conductance of the potassium ion channels will increase, and the Hodgkin-Huxley model will exhibit that the n curve will exhibit greater slopes, causing the repolarization stage of the action potential curve to occur in a shorter amount of time.

3.2 Methodology

A frog heart was prepared prior to the lab session with voltage-sensitive dye that illuminates with change in voltage.



Figure 3.1: Frog heart with stimulator at the apex.

The heart is submerged in three solutions: low-calcium Tyrode, Octopamine (10^{-4} M concentration), and Cromakalim (2×10^{-5} M concentration). For each of the solutions, the heart is pinned to the petri dish with the stimulation pins located at the apex of the heart. A green light and camera setup is created around the heart to ensure the photoreponse from the voltage-sensitive dye is visible.

The frog heart is stimulated with 4-ms duration, 60 V signal of frequencies varying from 0.5 events per second to 2.5 events per second. A picture of the heart is shown below in figure 3.1.

The data is processed using methods such as time averaging, spatial averaging, removing drift artifact. For time averaging the sigma value is 4 and the radius is 3. For spatial averaging, the sigma value is 8 and the radius is 6. Drift is removed by varying the period parameter between 500 and 800 ms. Restitution plots are created using .csv files generated from the processed data.

3.3 Results

From the action potential data observed in the experiments, we calculate the APD and DI to plot the restitution curves for each of the three cases. A direct comparison of the obtained restitution curves is shown in the figure below. A more detailed description of the plots for each solution is described in the following subsections.

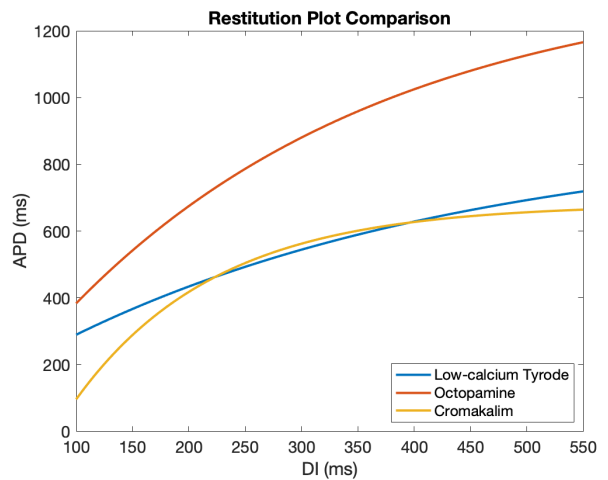


Figure 3.2: Restitution plots obtained for low-calcium Tyrode, Octopamine, and Cromakalim solutions.

3.3.1 Low-calcium Tyrode

Between all stimulation frequencies, the average APD is 547.5 ms, and the average DI is 436.66 ms.

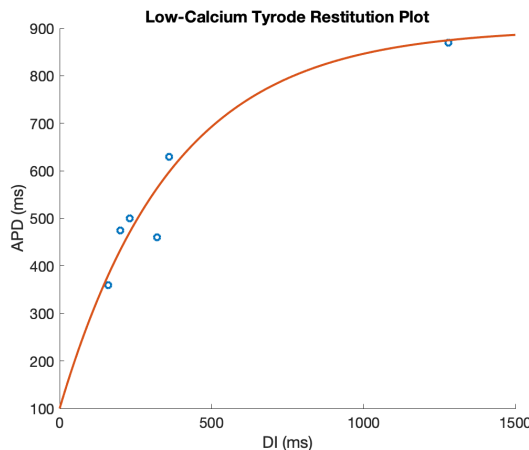


Figure 3.3: Restitution plot obtained while the frog heart is submerged in low-calcium Tyrode solution. The fitted curve is represented by the following expression: $900 - 800e^{-0.0027x}$.

3.3.2 Octopamine

Between all stimulation frequencies, the average APD is 754.22 ms, and the average DI is 317.55 ms.

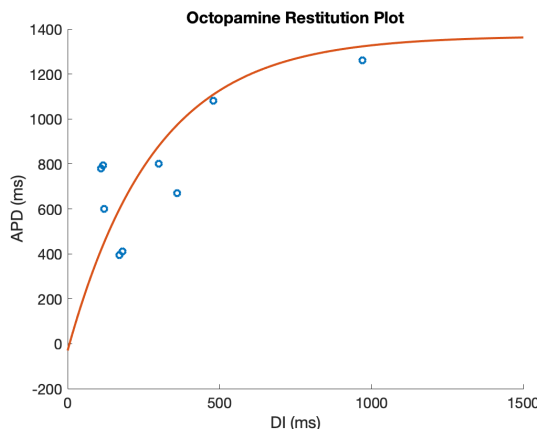


Figure 3.4: Restitution plot obtained while the frog heart is submerged in Octopamine. The fitted curve is represented by the following expression: $1370 - 1400e^{-0.0035x}$.

3.3.3 Cromakalim

Between all stimulation frequencies, the average APD is 544.37 ms, and the average DI is 333.37 ms.

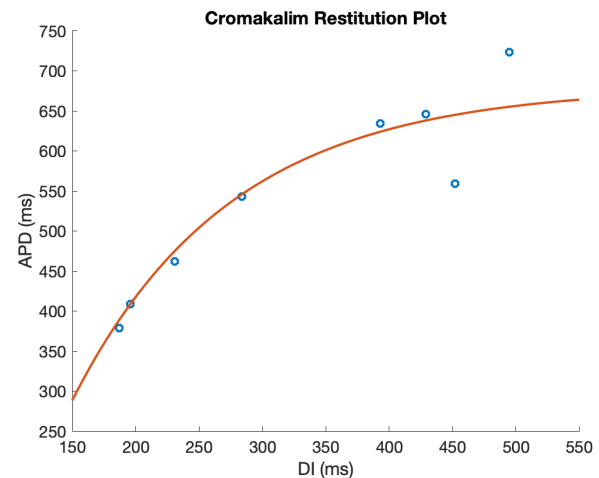


Figure 3.5: Restitution plot obtained while the frog heart is submerged in Cromakalim. The fitted curve is represented by the following expression: $680 - 1300e^{-0.008x}$.

3.4 Discussion

The original hypotheses were (1) when the heart is submerged in Octopamine, the action potential duration will increase and that the peak amplitude of the action potential will increase, and (2) when the heart is submerged in Cromakalim, the APD will decrease and the action potential frequency will also increase.

Regarding the first hypothesis, an explicit conclusion can be made about an increase in APD since the average APD increased by 206.72 ms when compared to the results obtained using low-calcium Tyrode solution. The average DI decreased by 119.11 ms, and the overall period increased on average by approximately 87.61 ms. This increase in APD is shown clearly in Figure 3.2, depicted by an upward

shift in the curve. The effect of the increase in extracellular calcium ion concentration can be observed from the Octopamine action potential curves, shown in Figure 3.7 in the Appendix section. Calcium dynamics are observed whereas the other plots, Figures 3.8 and 3.6, do not exhibit this quality. This additional upswing on the action potential plot increases the average action potential voltage. Unfortunately, a shift in maximum action potential voltage cannot be observed using the optical measurement method.

Addressing predictions made regarding the introduction of Cromakalim, the action potential duration did not change significantly; however, the overall action potential firing frequency did decrease. Introducing Cromakalim to the heart only decreased the average APD by 3.13 ms. The average DI decreased by 103.29 ms, which is the primary contributor to the increase in the action potential firing frequency. Overall, the average action potential firing period decreased by 106.42 ms, which supports the hypothesis. However, the rationale for the hypothesis was not supported by the data since it was presumed that the an increased rate of opening of potassium ion channels would decrease the APD, rather than the DI.

Unfortunately, no bifurcation points were observed using the optical measurement method so the obtained data set for all solutions is not an optimal representation.

Some factors that may have led to differences between the literature and the results obtained in this experiment are that the action potentials of vertebrates other than frogs were used in the listed studies.

Additional points of error include inconsistent perfusion of the solutions as well as varying soak

times before obtaining the data. For example, the time between substituting Cromakalim for Octopamine was far greater than the time between substituting the Octopamine for the low-calcium Tyrode. Additionally, an uneven number of trials for obtaining data points for the restitution plots were used between the solutions. Also, the low-calcium Tyrode solution data was lost for the frog heart used for to obtain data with the Octopamine and Cromakalim solutions. The low-calcium Tyrode solution data was obtained from another group.

Key points of improvement if another iteration of the experiment were to be performed in the future would be to address the points of error listed above, as well as utilizing a different stimulator to more precisely adjust the stimulation frequency since the stimulator used for these experiments used only an analog dial. Additionally, with greater precision stimulator, it may be easier to obtain the bifurcation points.

3.5 Conclusion

Ultimately, it was found that Octopamine increased the frog heart APD by approximately 206 ms, which supports the first hypothesis. The average DI decreased by approximately 120 ms. Octopamine did introduce calcium dynamics to the action potential plots, resulting in an increase in average action potential voltage over time.

The introduction of Cromakalim decreased the average action potential firing period of the frog heart by approximately 106 ms, which supports the second hypothesis regarding an increase in firing rate. The average APD decreased by approximately 3 ms and the average DI decreased by 103 ms.

3.6 Appendix

Action potential data for each of the solutions: Cromakalim, Octopamine, and low-calcium Tyrode.

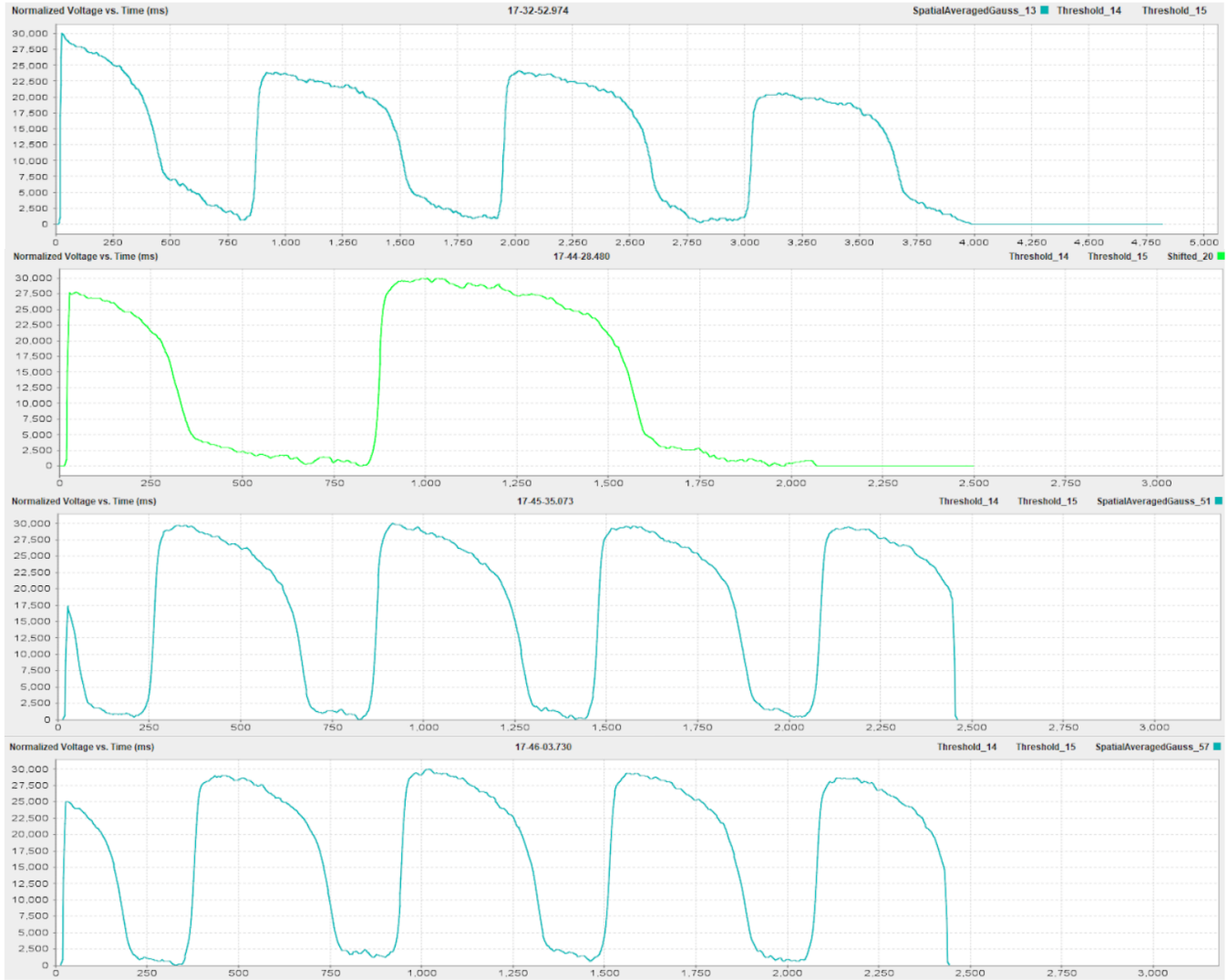


Figure 3.6: Action Potential response for frog heart submerged in Cromakalim when stimulated externally at the apex of the heart.

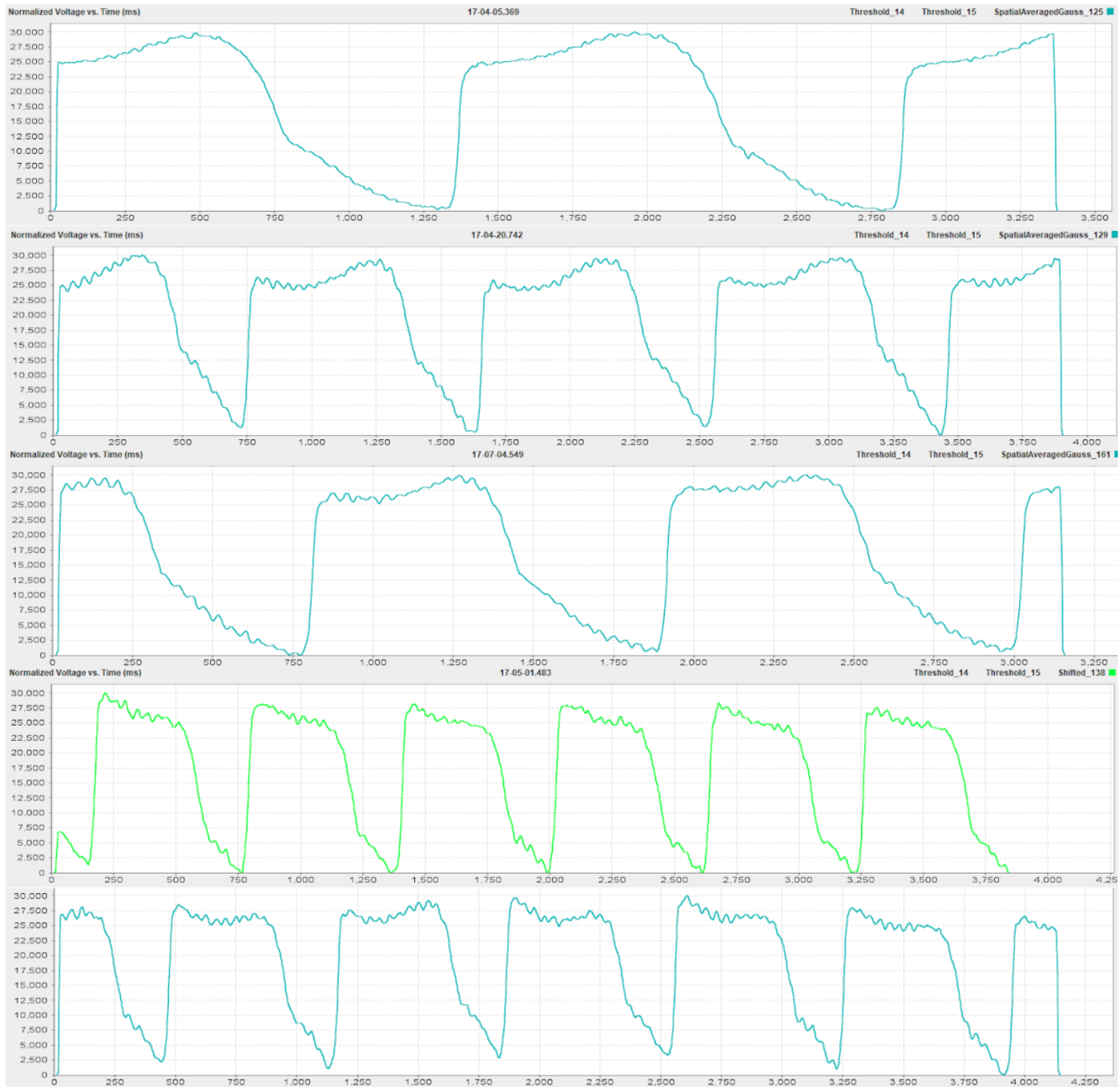


Figure 3.7: Action Potential response for frog heart submerged in Octopamine when stimulated externally at the apex of the heart.

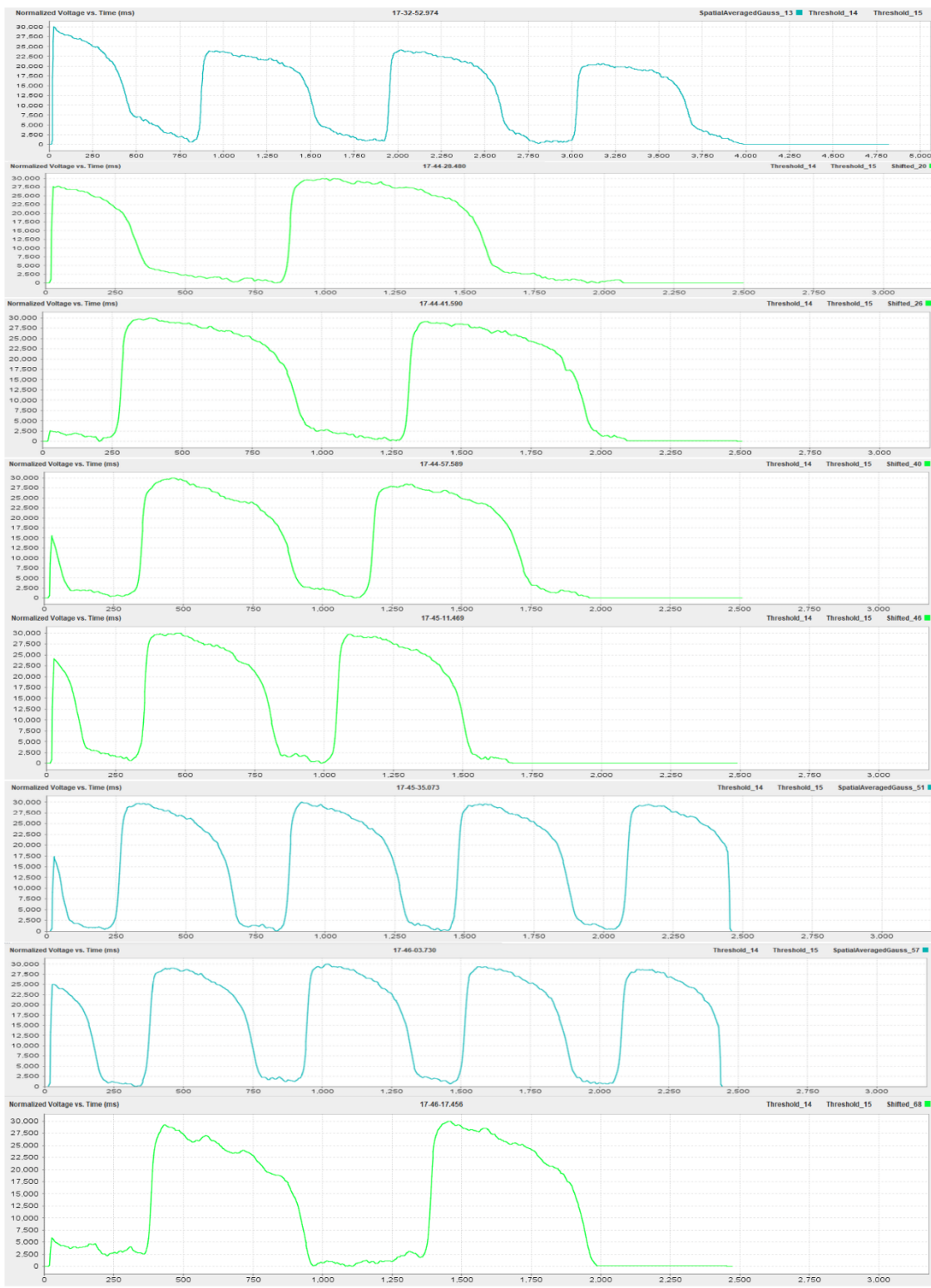


Figure 3.8: Action Potential response for frog heart submerged in low-calcium Tyrode when stimulated externally at the apex of the heart.

References

- [1] Takayoshi Ubuka. Octopamine. *Handbook of Hormones*, 2, 2020.
- [2] E A Shinebourne, M L Hess, R J White, and J Hamer. The effect of noradrenaline on the calcium uptake of the sarcoplasmic reticulum. *Cardiovascular Research*, 3(2):113–117, 1969.
- [3] Kara Rogers. Norepinephrine. *Encyclopedia Britannica*, 2017.
- [4] J Quadbeck and M Reiter. Cardiac action potential and inotropic effect of noradrenaline and calcium. *Naunyn-Schmiedeberg's Archives of Pharmacology*, 286:337–351, 1975.
- [5] Hiroshi Yamagishi. Aminergic modulation of the myogenic heart in the branchiopod crustacean *triops longicaudatus*. *Zoological Science*, 20, 2003.
- [6] K Shigenobu, C Kageyama, and M Watanabe. Action potential shortening and negative inotropic effects of a novel potassium channel opener, nip-121, as compared with cromakalim in guinea pig ventricular myocardium. *Jpn J Pharmacol.*, 57(1):111–121, 1991.

Makin' Music with Crayfish

Lynn Jin
Zach Mobille
Ressa Reneth Sarreal
Biswadeep Chakraborty

March 28, 2022

Abstract

A reverse correlation analysis is performed on extracellular measurements of neurons from the muscle receptor organs (MROs) in the crayfish. During the experiment, various stimuli were exerted on the MROs. These data are processed to obtain a function characterizing the receptive field of the nerve. It is shown that a white-noise stimulus is more effective than a ramping stimulus, as measured by errors between the original response and the reconstructed one.

Introduction

- ▶ The firing rate of a neuron is typically not an instantaneous function of the stimulus strength, but rather depends on a period of time before a given spike.
- ▶ For a time-dependent stimulus $s(t)$ evoking n spikes at times t_i ($i = 1, \dots, n$), the **spike-triggered average** (STA) $C(\tau)$ is defined as:

$$C(\tau) = \left\langle \frac{1}{n} \sum_{i=1}^n s(t_i - \tau) \right\rangle$$

where angled brackets denote the average over all trials [2].

- ▶ The **muscle receptor organs** (MROs) of the crayfish are neurons that sense and encode joint position and stretch. [3].

Mathematical Background

- ▶ An estimate of the firing rate r_{est} is:

$$r_{\text{est}}(t) = r_0 + \int_0^{\infty} D(\tau) s(t - \tau) d\tau$$

r_0 is the background firing rate, s is the stimulus, $D(\tau)$ weights how strongly the firing rate at time t is affected by the stimulus at time $t - \tau$.

- ▶ Choose the D that minimizes the average mean-squared error E between the predicted rate r_{est} and the measured rate r :

$$E = \frac{1}{T} \int_0^T [r_{\text{est}}(t) - r(t)]^2 dt$$

where T is the duration of the trial.

Mathematical Background (continued)

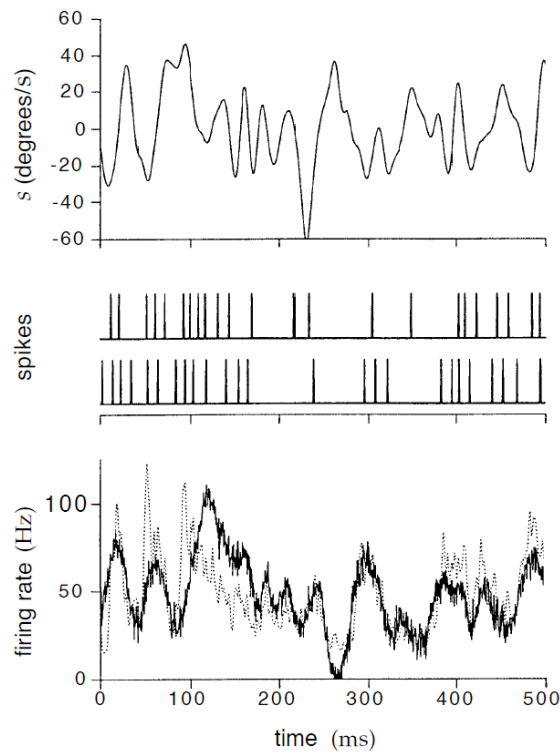
- ▶ The error E is most readily minimized when the stimulus is white noise. In this case, The kernel D that does the trick is

$$D(\tau) = \frac{\langle r \rangle C(\tau)}{\sigma_s^2}$$

where σ_s characterizes the variability of the stimulus, $\langle r \rangle$ is the average firing rate, and $C(\tau)$ is the STA.

- ▶ There is a more complicated formula for $D(\tau)$ when the stimulus is arbitrary.

Schematic of Reverse Correlation Method



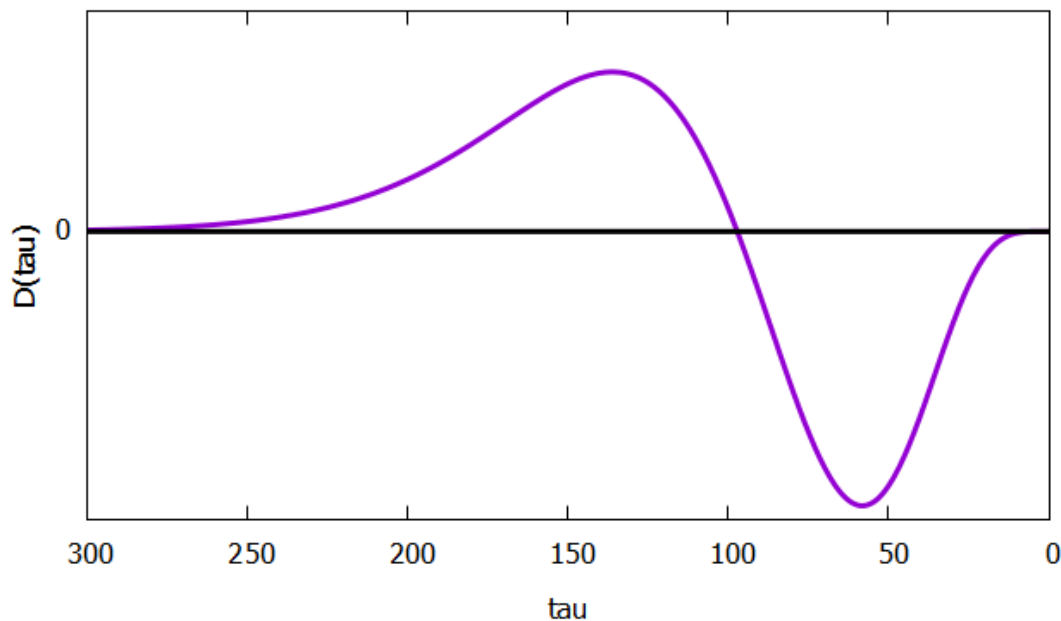
Dark trace = reconstructed firing rate using the reverse correlation method

Light trace = Experimentally-measured firing rate

¹Dayan & Abbott (2005)

Hypothesis

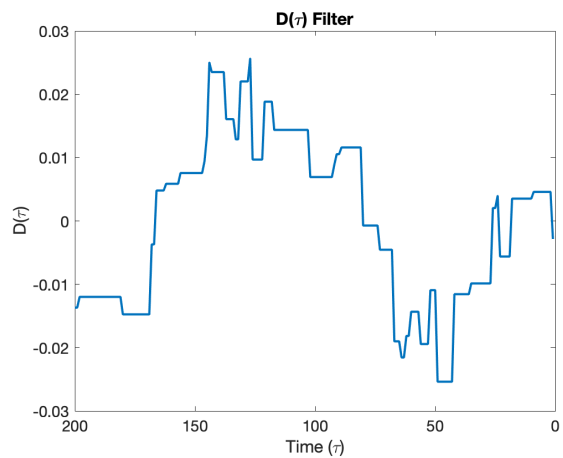
- ▶ The mean squared error between the estimated firing rate and the measured firing rate is lower for a white noise stimulus than for a ramp stimulus experiment with the MROs.
- ▶ Based on biological intuition, the receptive field should look somewhat like:



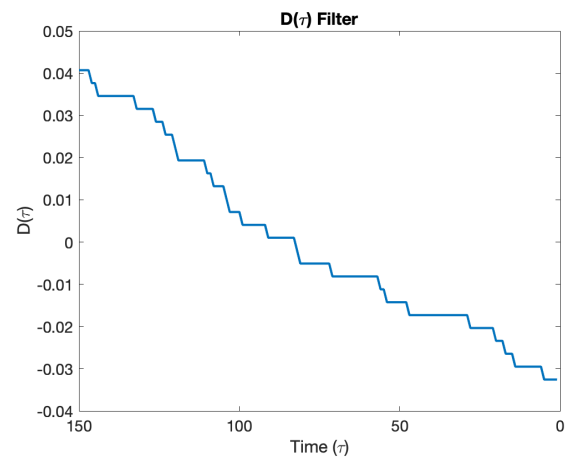
Methodology

1. Dissect the crayfish and access MROs.
2. Program the motor to provide a stimulus to the crayfish tail.
3. Record stimulus (input to the motor) and the MRO response for the following stimuli:
 - ▶ White noise, 2.5 Hz, 0-90 degrees
 - ▶ Ramp (5 s) and hold (10 s)
4. Process the data to predict the firing rate.
 - 4.1 Identify spikes.
 - 4.2 Observe the corresponding stimulus for a window of τ seconds prior to the spike.
 - 4.3 Calculate the STA of the subset. Then calculate $D(\tau)$.
 - 4.4 Convolve $D(\tau)$ with a pre-processed stimulus $f(s(t - \tau))$ to obtain the estimated firing rate, $r(t)$.
 - 4.5 Compare the estimated firing rate with experimental firing rate.

Receptive Fields

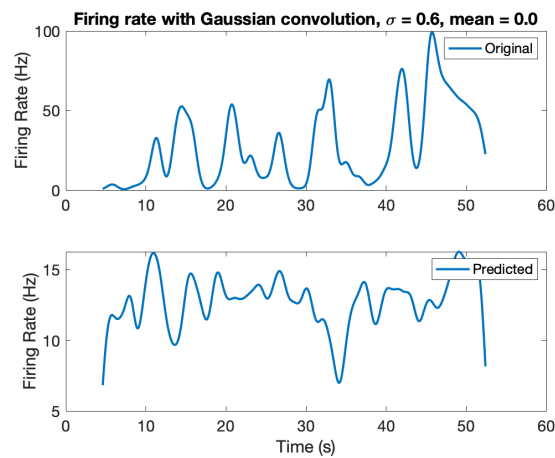


(a) White Noise

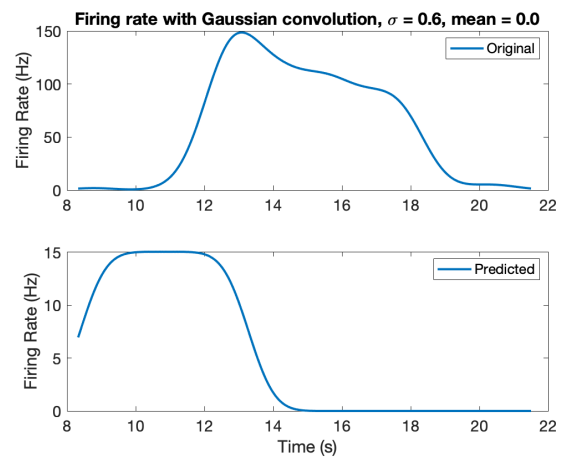


(b) Ramp Function

Reconstructed Firing Rates

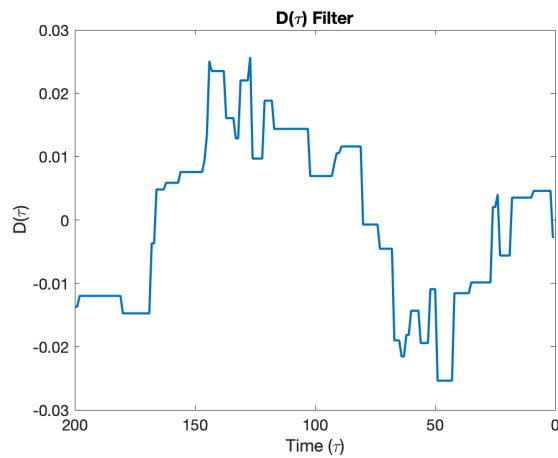


(c) White Noise

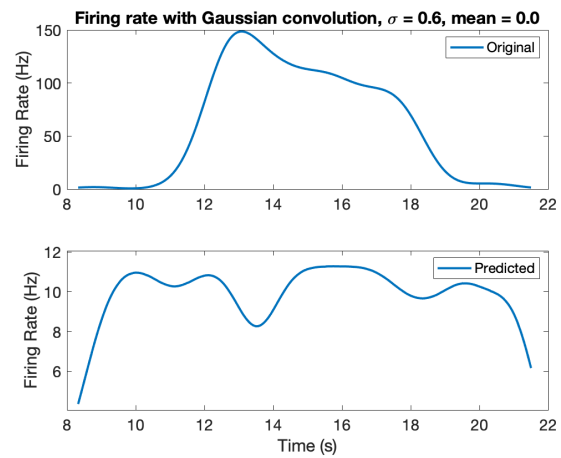


(d) Ramp Function

Reconstructed Firing Rates



(e) White Noise Kernel



(f) Estimated Firing Rate for Ramp Function using White Noise Kernel

Summary of Results

For model evaluation, we use the RMSE error (discussed above) and the log-likelihood. [1].

The log-likelihood is given as

$$\log \mathcal{L} = \sum_t (n(t) \log(r(t)\Delta t) - r(t)\Delta t)$$

where $r(t)$ is the predicted response of the model.

To estimate a lower bound on the log-likelihood, form a null hypothesis as:

$$\log \mathcal{L}_{\text{null}} = \sum_t (n(t) \log(\langle n(t) \rangle) - \langle n(t) \rangle)$$

	RMSE	Log-Likelihood
White Noise	28.92	0.884
Ramp Signal	76.86	0.228
Ramp with White Noise Kernel	72.16	0.698

Discussion

- ▶ The reconstructed response for the white noise stimulus has a lower error than that of the ramp stimulus.
 - ▶ They are off by some scale factor, which could be accounted for by the background firing rate r_0 .

Conclusion

- ▶ A white noise stimulus is superior for exploring the space of all possible inputs than a ramping stimulus.
- ▶ Reverse correlation analysis is most successful for reconstructing receptive fields when the stimulus is white noise.

References

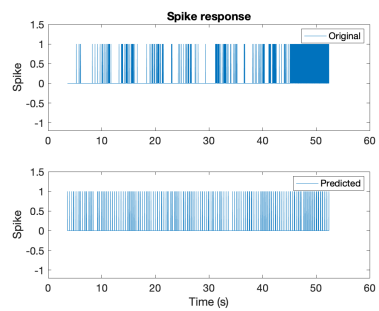
-  Johnatan Aljadeff, Benjamin J Lansdell, Adrienne L Fairhall, and David Kleinfeld.
Analysis of neuronal spike trains, deconstructed.
Neuron, 91(2):221–259, 2016.
-  Peter Dayan and Laurence F Abbott.
Theoretical neuroscience: computational and mathematical modeling of neural systems.
MIT press, 2005.
-  Bonnie Leksrisawat, Ann S Cooper, Allison B Gilberts, and Robin L Cooper.
Muscle receptor organs in the crayfish abdomen: a student laboratory exercise in proprioception.
JoVE (Journal of Visualized Experiments), (45):e2323, 2010.

Thank you!

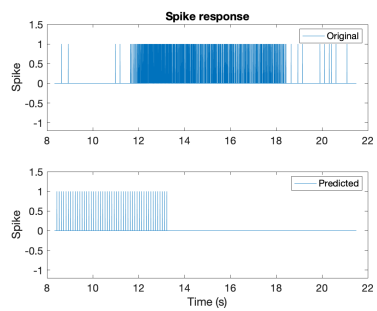
Questions?



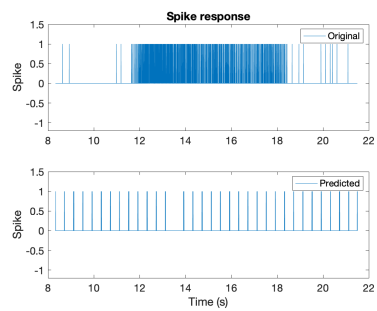
Supplementary Results



(g) White Noise



(h) Ramp Function



(i) Ramp Function with
Noise Kernel

Figure: Observed and Estimated Spikes

Lab Report 5: Fitts' Law Adaptation to Observe Effects of Simultaneous Tasks on Information Processing Rate

Ressa Reneth Sarreal, Biswadeep Chakraborty, Lynn Jin, Zachary Mobile

PHYS 4250/8814

April 6, 2022

Abstract- We explore how information processing rate will be affected when simultaneous tasks are performed. Using a common Fitts' law experimental setup for the control trials, a subject must perform an alternating target task at various indices of difficulty. In another set of trials, an additional random character identification task is performed at the same time as the primary task. Information processing rate is calculated to directly compare how performing the simultaneous tasks affects the primary task performance. Results show that the processed information of the primary task decreases by approximately 136.5 bits when performing the simultaneous character identification task.

5.1 Introduction

The primary goal for the experiment depicted in this document is to observe how information processing rate changes when multiple simple tasks are performed simultaneously. We hypothesize that a subject who performs an additional simple task to an alternating target task, the information processing rate will decrease by a minimum information rate necessary to process the additional task.

Tsang and Wilson describe how increasing mental workload can lead to a decrease in performance [1]. In providing an additional task for the subject to perform, we foresee that the performance in the primary task will decrease, in agreement with Tsang and Wilson's findings.

Specifically, based on calculations of information rate and introducing a factor where information rate, or entropy, may be calculated, we have a supplementary hypothesis that the user will have a decrease in

information rate at a minimum value of the information rate. Information, H , can be calculated in equation 5.1, where k is 1, a is 2 (both per Shannon's theorem), N is the total number of states, and P_i is the probability of each state, i .

$$H = -k \sum_{i=1}^N P_i \log_a (P_i) \quad (5.1)$$

5.2 Methodology

A simple motor task of hitting two alternating targets using a Wacom tablet stylus was performed by a subject to observe how movement time is affected by performing variations of the task at different indices of difficulty. Fitts' index of difficulty is calculated using equation 5.2 [2], and information rate is measured in equation 5.3. A_e and W_e are the effective amplitude and effective width values of the targets

used to adjust the index of difficulty. Effective amplitude is the distance consecutive between extrema, and effective width is $2 \times 1.96 \times$ the average standard deviation at both extrema. These values are obtained and calculated using the stylus tracking software on the Wacom tablet during each trial then processing the data in MATLAB.

$$ID = \log_2(N) = \log_2\left(\frac{2A_e}{W_e}\right) \quad (5.2)$$

$$I_p = \left(\frac{1}{T_M}\right) \log_2\left(\frac{2A_e}{W_e}\right) \quad (5.3)$$

The subject was asked to alternate between two targets as quickly as possible for 30 seconds. The amplitudes and widths of the targets are adjusted to obtain ID values between 2 and 7. The ID values were altered by varying general amplitude, A, and width, W, shown in Figure 5.1. These values are used to approximate ID before each trial was performed. This data set will be used as a control.

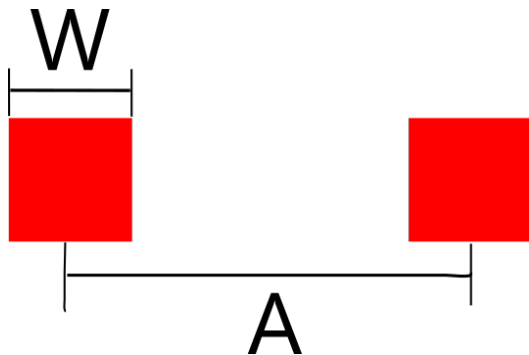


Figure 5.1: Graphical definition of the width W and amplitude A in the Fitts law formula 5.2.

A similar set of trials was performed; however, in addition to the simple alternating target task, the subject was asked to identify alphabetical charac-

ters that periodically appeared on a separate monitor. These characters appeared for one second and disappeared for one second before another random character would then appear. This cycle would repeat until the end of the task. Each trial lasted 30 seconds, the same duration of the control trials. The amplitudes and widths of the targets varied identically to the control values to obtain the same ID values. The setup is depicted in Figure 5.2. Additionally, the information rate of the presented characters is constant for each trial. Information presented during each 30 second trial is 4.7 bits \times 15, which is the number of times a random character is presented. In total, approximately 70.5 bits of information are presented during each character identification task (across 30 seconds).

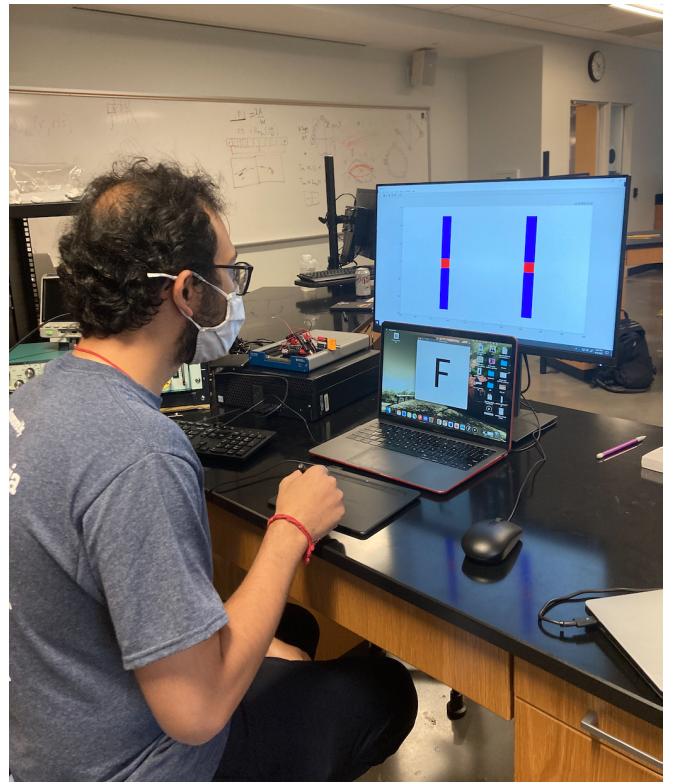


Figure 5.2: Experimental setup of the subject simultaneously performing the alternating target task and the alphabet character identification task.

5.3 Results

The breakdown of movement time, acceleration time, and deceleration time are presented for the control trials and the trials with the additional letter identification tasks, Figures 5.3 and 5.4 respectively. Information processed for each of the trials are plotted in Figure 5.6. The information processing rate for each planned ID trial is shown in Figure 5.5. The amount of information processed is calculated as the information rate, equation 5.3, multiplied by 30 seconds, the duration of each trial.

Our hypothesis was that the trials performed with the added distraction of having to identify and recite letters once every other second yield a lower information processing rate when compared to the information processing rate observed from the control.

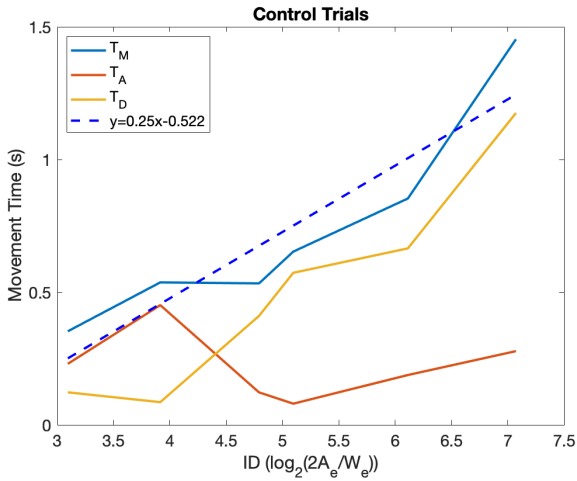


Figure 5.3: Control trials movement times per effective index of difficulty, as well as the break down of movement time into acceleration time and deceleration time. The linear approximation curve has an r^2 value of 0.8516.

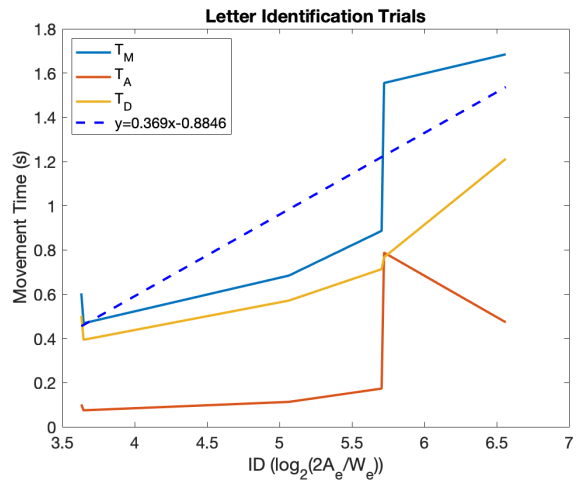


Figure 5.4: Additional letter identification task trials movement times per effective index of difficulty, as well as the break down of movement time into acceleration time and deceleration time. The linear approximation curve has an r^2 value of 0.7335.

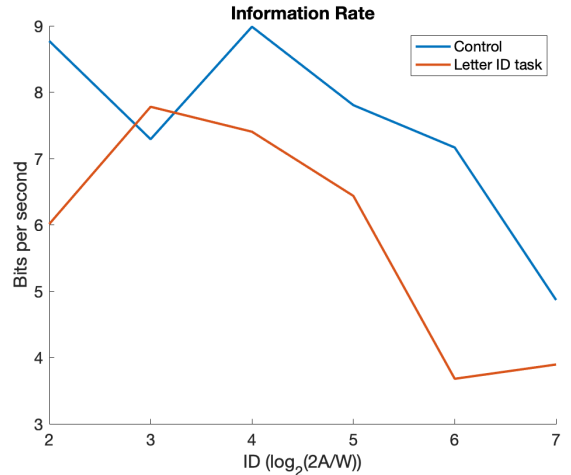


Figure 5.5: Information processing rate over each trial.

The validity of this hypothesis is confirmed by comparing the average information processing rate of 7.48 bits/s in the control case (Figure 5.3) with 5.86 bits/s in the distracted case (Figure 5.4). The difference between the two averaged processing rates is 1.62 bits/s. From Figure 5.6 an average of

136.5 more bits were processed when the subject did not have to perform the additional identification task, which is greater than the predicted minimum information value of 70.5 bits.

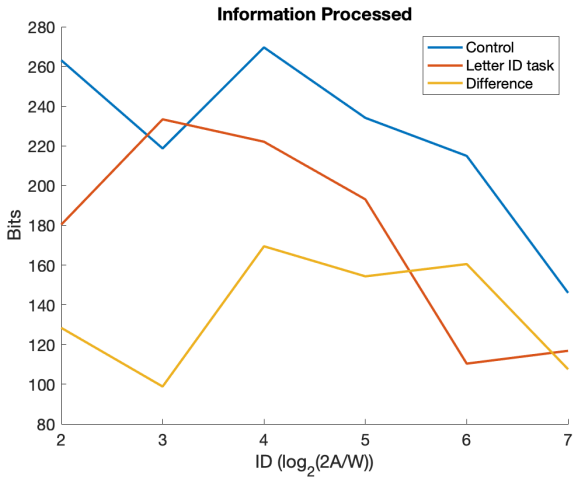


Figure 5.6: Information processed over each trial and the difference of information processed for each corresponding trial ID.

5.4 Discussion

The primary hypotheses was that a subject who simultaneously performs an additional simple task to an alternating target task, one generally used to test Fitts' Law, the information processing rate will decrease. The secondary hypothesis was that the information processing rate will decrease by a minimum calculated information rate that would be necessary to process the additional task.

Regarding the primary hypothesis, a clear decrease in information processing rate is observed in Figure 5.5 with the exception of when the target ID is 3. Reason for this error may be due to one or more of the following: (1) the subject having inconsistent hand positions between trials, (2) the subject shifting the setup to become more comfortable

between trials, (3) the subject adjusting their distance and perspective to the monitor between trials, (4) the subject having an awareness of the different regimes possible for performing the primary task, (5) the subject's focus between the easier trials varied (it was visibly obvious during an ID=2 trial, the subject was very relaxed but for an ID=3 trial, the subject was very motivated to go as fast as possible). These points of error seemed to affect the plots of the break down of movement time into acceleration and deceleration time as well, Figures 5.3 and 5.4.

Regarding the secondary hypothesis, the difference in average information processed between the control trials and the additional identification task trials is approximately 136.5 bits, which is almost twice the predicted minimum value of 70.5 bits. A minimum value, rather than an exact value, was predicted because it was presumed that some information would also be lost when the subject transitioned between tasks. The secondary hypothesis and rationale behind the hypothesis seem to be supported from the obtained data set.

Key points of improvement if another iteration of the experiment were to be performed in the future would be to better control the subject such that their position and movement scheme (wrist movements, having the wrist rested on the table, etc) is consistent between trials. Additionally, a subject who is unaware of fixed point or limit cycle regimes would be selected. Finally, more trials at all IDs between 2 and 7 would be performed.

Other interesting points to explore would be to vary the additional tasks that are simultaneously performed with the primary task to observe how and what amount of information is lost during the transition between tasks.

5.5 Conclusion

Ultimately, it was found that performing a simultaneous task reduces the information processed during the primary task. The amount that the processed information decreased is a minimum value of the information produced by the secondary task.

Specifically, in performing the primary task of alternating between two targets, a common setup for testing Fitts' Law, as well as simultaneously performing a secondary task of verbally identifying alphabet characters, where a random one is presented every other second, the information processed decreases by 136.5 bits over a 30 second trial.

References

- [1] Pamela S Tsang and Glen B Wilson. Mental workload measurement and analysis. *Handbook of human factors and ergonomics*, 2:417–449, 1997.
- [2] Paul M Fitts. The information capacity of the human motor system in controlling the amplitude of movement. *Journal of experimental psychology*, 47(6):381, 1954.

Final Report: From intracellular to extracellular dynamics in electrically-active biological systems

Zach Mobile and **Ressa Reneth Sarreal**

Georgia Institute of Technology, Atlanta, GA 30332

April 29, 2022

Abstract

We explore how to develop a model for extracellular action potential recordings. Using the Beeler-Reuter model to obtain baseline, intracellular parameters, a multi-compartmental, Beeler-Reuter-based model was developed by combining with work by Einevoli et al. A qualitative comparison between experimental and simulated data of extracellular and intracellular recordings was made by creating a normalized voltage vs. phase plots for each of the recorded action potentials. The mean-squared error was calculated between each experimental-simulated data pairs. Additionally, the model was further validated by appropriately adjusting the model parameters to align with data obtained when K^+ and Na^+ ion channel blockers are introduced to the experimental setup of the heart. The qualitative comparison resulted in a MSE of 0.0041 mV^2 for intracellular, low-calcium Tyrode recordings and a MSE of 0.0051 mV^2 for extracellular, low-calcium Tyrode recordings.

1 Introduction

The ability to infer an intracellular response from an extracellular measurement or an extracellular response from an intracellular measurement is useful for working with neural systems and applications, especially if neural recording methods are limited. We hypothesize that a multicompartmental, Beeler-Reuter-based model can accurately represent extracellular potential of cells located in a frog ventricle. Furthermore, adjustments to membrane conductance values will accurately correspond with the effects of introducing ion channel blockers.

Models, such as Hodgkin-Huxley (HH) and Beeler-Reuter (BR), have exhibited success in representing intracellular recordings of various neurons. The BR model was developed as an extension of the HH model to incorporate Calcium dynamics into the model [1]. The BR model of ventricular myocyte dynamics [2], explained by equations [1] through [3] is made of eight-variables, six of which are gating variables. The incorporation of Calcium currents into the model is useful for emulating action potentials of cardiac cells. Though these models are helpful for predicting intracellular neuron responses, modeling tools for extracellular response models are lacking in comparison.

In applications where obtaining intracellular recordings is challenging or impossible, the capability to relate extracellular signals to intracellular action potentials would prove useful. We are motivated to emulate the collective dynamics of electrically-active physiological systems, which is dependent on contributions from multiple units, or a small area of cells. Additionally, single intracellular recordings are limited in their ability to capture collective dynamics; furthermore, a mapping from the intracellular activity of a small group of cells to the resulting extracellular voltage would capture these dynamics.

Using the BR model combined with work from Einevoli et al. [3], an extracellular response model can be formed. In addition to creating the model, intracellular recordings will be captured from a frog ventricle, in addition to extracellular recordings. Model parameters will be adjusted to best fit the experimental data; furthermore, the model will be validated by adjusting ion channel currents and conductance values to match recordings obtained when the heart

is submerged in low-Calcium Tyrode solution as well as when ion channel blocker solutions are introduced to the frog ventricle.

2 Methodology

For the purpose of this project, attempts were made to obtain recordings from the sciatic nerve of a bull frog. Nerve responses were not obtained during these attempts, but will be further detailed in the following section. Sciatic nerve recordings will not be mentioned further in the document.

Ultimately ventricular recordings from a frog heart were used to approach the hypothesis, which will be described in Section 2.4.

2.1 Sciatic nerve recordings

The sciatic nerve was carefully dissected from a bull frog. The lower extremities of the bull frog were severed such that the lower part of the pelvic region and the two legs were attached. Then, layers of muscle were removed to access the sciatic nerve by the femur and the tibiofibula. The nerve is shown in Figure 2.1

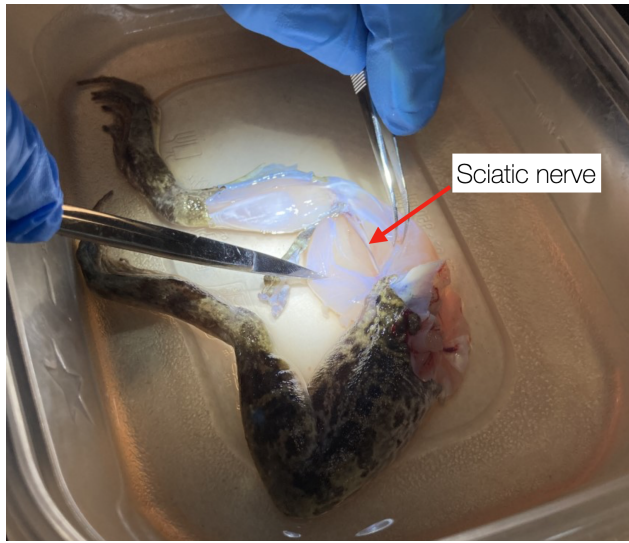


Figure 1: Dissection of the frog legs to access the sciatic nerve.

A 1-ms pulse of 100 V at various frequencies [4] were applied to the sciatic nerve near the upper femur by inserting conductive insect pins into the nerve such that the pos-

itive terminal is proximal to the ground terminal. During stimulation, the gastrocnemius muscle exhibited contractions. However, using several methods of obtaining extracellular nerve responses, little to no response was observed.

Methods for obtaining the extracellular nerve response from the sciatic nerve include inserting insect pins on opposite sides of the nerve, draining the Tyrode solution. Some small response was observed as a down-swinging spike; however, the signal was not constantly present and difficult to discern as a nerve response. The pins were also then inserted into the nerve for recording, but this attempt did not exhibit any response. Similarly, no recordings were obtained when using a suction electrode of varying glass-pipette diameters.

It is possible that the nerve response occurred in a different region of the sciatic nerve during stimulation and the suction electrode only covered a localized region that did not exhibit the electrical signals. The insect pins method in capturing evoked changes in electric fields did not capture the response possibly because the pins were not close enough to the nerve or the stimulator was generating too much noise, making it difficult to notice any response.

2.2 Intracellular modeling

The Beeler-Reuter model of ventricular myocytes [2][5], described below, is used to model single cells in the frog heart:

$$C \frac{dV}{dt} = I_{app}(t) - I_{Na} - I_K - I_{Ca} \quad (1)$$

$$\frac{dc}{dt} = 0.07(1 - c) - I_{Ca} \quad (2)$$

$$\frac{dy}{dt} = \alpha_y(1 - y) - \beta_y y \quad (3)$$

V is the intracellular voltage and $c = 10^7 \times [\text{Ca}]_i$ where $[\text{Ca}]_i$ is intracellular concentration of Ca^{2+} . The variable y is indexed and encapsulates all of the gating variables $y = m, h, j, d, f, x$, so this is an 8-dimensional system of differential equations. It is non-autonomous when the ap-

plied current I_{app} is not identically zero.

The gating variables govern the dynamics of the currents I_{Na} , I_{K} , and I_{Ca} . The sodium current has the form

$$I_{\text{Na}} = (g_{\text{Na}}m^3hj + g_l)(V - E_{\text{Na}})$$

where g_{Na} is the sodium conductance, g_l is the leak conductance, and E_{Na} is the Nernst potential for sodium. The potassium current I_{K} has two parts:

$$I_{\text{K}} = I_{\text{K},\infty}(V) + I_x$$

where $I_{\text{K},\infty}(V)$ is an instantaneously-activating component (see refs. [2] [5] for the exact form) and I_x is the time-dependent component with the form

$$I_x = g_x x \frac{\exp[0.04(V + 77)] - 1}{\exp[0.04(V + 35)]}$$

where g_x is a potassium conductance. The calcium current has the form

$$I_{\text{Ca}} = g_{\text{Ca}}fd(V + 82.3 + 13.0287\ln[\text{Ca}]_i)$$

where g_{Ca} is the calcium conductance. The voltage-dependent rates $\alpha_y = \alpha_y(V)$ and $\beta_y = \beta_y(V)$ both have the form

$$\frac{C_1 \exp\left(\frac{V-V_0}{C_2}\right) + C_3(V - V_0)}{1 + C_4 \exp\left(\frac{V-V_0}{C_5}\right)}$$

Using this model, intracellular voltage responses can be generated, as shown in Figure 2.2

All numerical simulations shown in this report have been computed with the Python module `scipy.integrate.odeint` with a time step of 0.1 ms.

2.3 Extracellular modeling

In this section, the Beeler-Reuter model is used to build a multi-compartment model for a very small patch of cardiac tissue. In particular, we study a 3×3 grid of Beeler-Reuter units and compute the extracellular voltage a distance away from the sheet of cells. Each point compartment of this model is treated as identical, based on the assumption that cells in a small area are of the same type. The computation

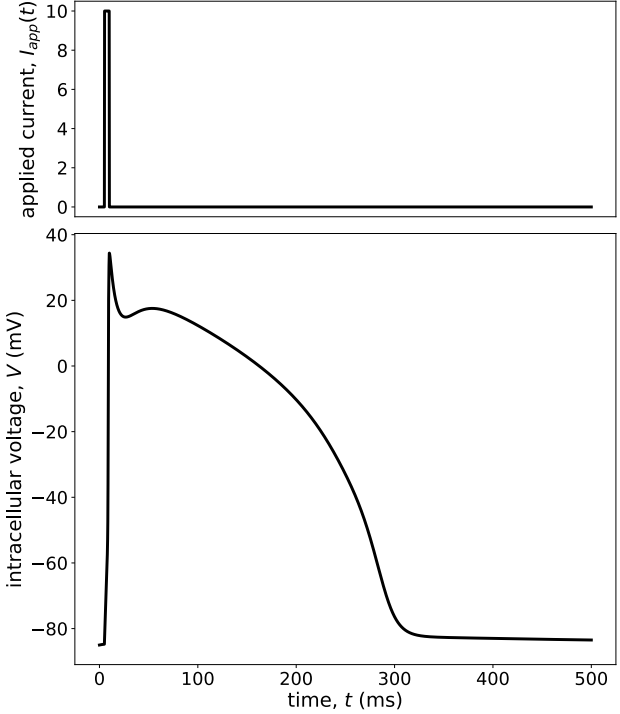


Figure 2: Intracellular potential predicted using the Beeler-Reuter model when an impulse of current is applied.

of extracellular voltage comes from volume conductor theory and assumes a quasistatic approximation of Maxwell's equations [6] to hold in the anatomical region of interest. This calculation also rests on the assumption that the extracellular medium has the same conductivity in all directions (it is isotropic). Following Nunez & Srinivasan, these assumptions result in Ohm's law $\mathbf{J} = \sigma \mathbf{E}$ to hold up to an additional macroscopic source current density \mathbf{J}_s . The relation between the electric field around the tissue \mathbf{E} and its total current density \mathbf{J} becomes [7]

$$\mathbf{J} = \sigma \mathbf{E} + \mathbf{J}_s \quad (4)$$

where σ is the extracellular, isotropic conductivity with units mS/cm. By substituting equation (4) into the continuity equation $\nabla \cdot \mathbf{J} = 0$ for purely resistive, linear extracellular media and writing the field as $\mathbf{E} = -\nabla V_e$, we eventually come to the expression for the extracellular volt-

age V_e

$$V_e(\mathbf{r}, t) = \frac{1}{4\pi\sigma} \sum_{n=1}^N \frac{I_n(t)}{R_n} \quad (5)$$

where $R_n = |\mathbf{r} - \mathbf{r}_n|$ is the distance between the n^{th} point source current located at \mathbf{r}_n and the electrode located at \mathbf{r} . The n^{th} point source current itself is given by $I_n(t)$. This equation for V_e only yields interesting results that are pertinent to an experiment involving tissue instead of single cells when the point source currents come from multiple sources at distinct locations. We thus study the multi-compartment model [8]; if compartment n is a member in a linear chain configuration of Beeler-Reuter units, then its voltage evolution follows:

$$g_{n,n+1}(V_{n+1} - V_n) - g_{n-1,n}(V_n - V_{n-1}) = C_n \frac{dV_n}{dt} + \sum_j I_n^j \quad (6)$$

The gating dynamics of the n^{th} compartment are not coupled to its neighbors. They follow equations 2 and 3 above, except with subscripts on the variables describing that compartment. The index j in the above expression is over the ion channels of the n^{th} compartment. Treating each compartment as a point, the contribution of current from the n^{th} compartment to the extracellular voltage in equation 5 is equal to the right-hand side of the voltage evolution (equation 6). Note that this sum of transmembrane currents includes the capacitive current of the n^{th} compartment $C_n \dot{V}_n$ where C_n is the membrane capacitance of the n^{th} compartment and V_n its intracellular voltage. We treat the coupling conductances as identical. Symbolically, $g_{n,m} \equiv g_c$ for any two coupled compartments n and m .

As mentioned above, the structure of the multicompartmmt model used here is a 3×3 lattice. This arrangement of heart cells is sketched below in figure 4. The coupling currents therein are defined as

$$\begin{aligned} I_{n,m} &= g_{n,m}(V_m - V_n) - g_{m,n}(V_n - V_m) \\ &= g_c(V_m - V_n) - g_c(V_n - V_m) \end{aligned}$$

Again, $I_n(t)$ are the point source currents at each compartment. In this preliminary model, current is injected at

compartment 1. The observed voltages at the nine compartments can be seen in Figure 5

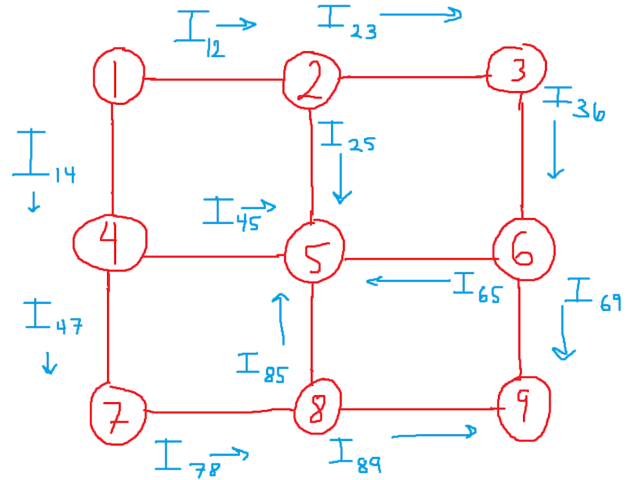


Figure 4: Current flow connections between the nine compartments for the extracellular BR-based model.

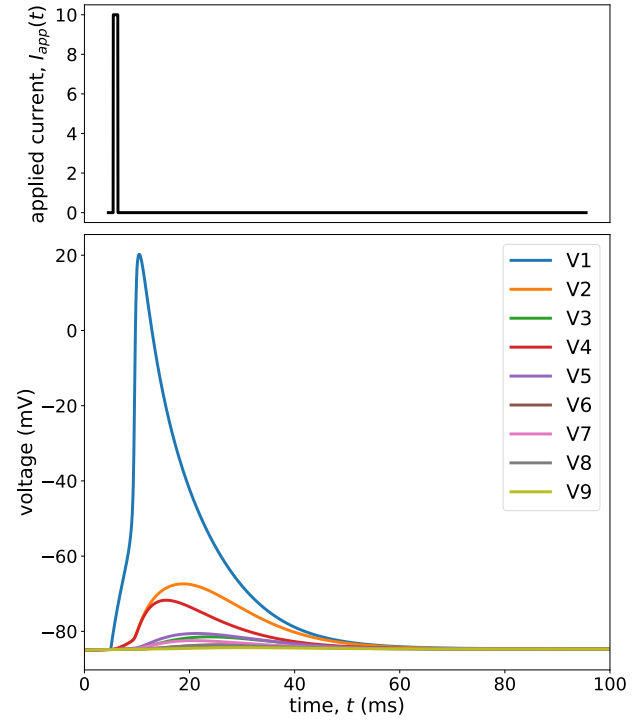


Figure 5: Observed voltages using the nine-compartment model at each of the compartments.

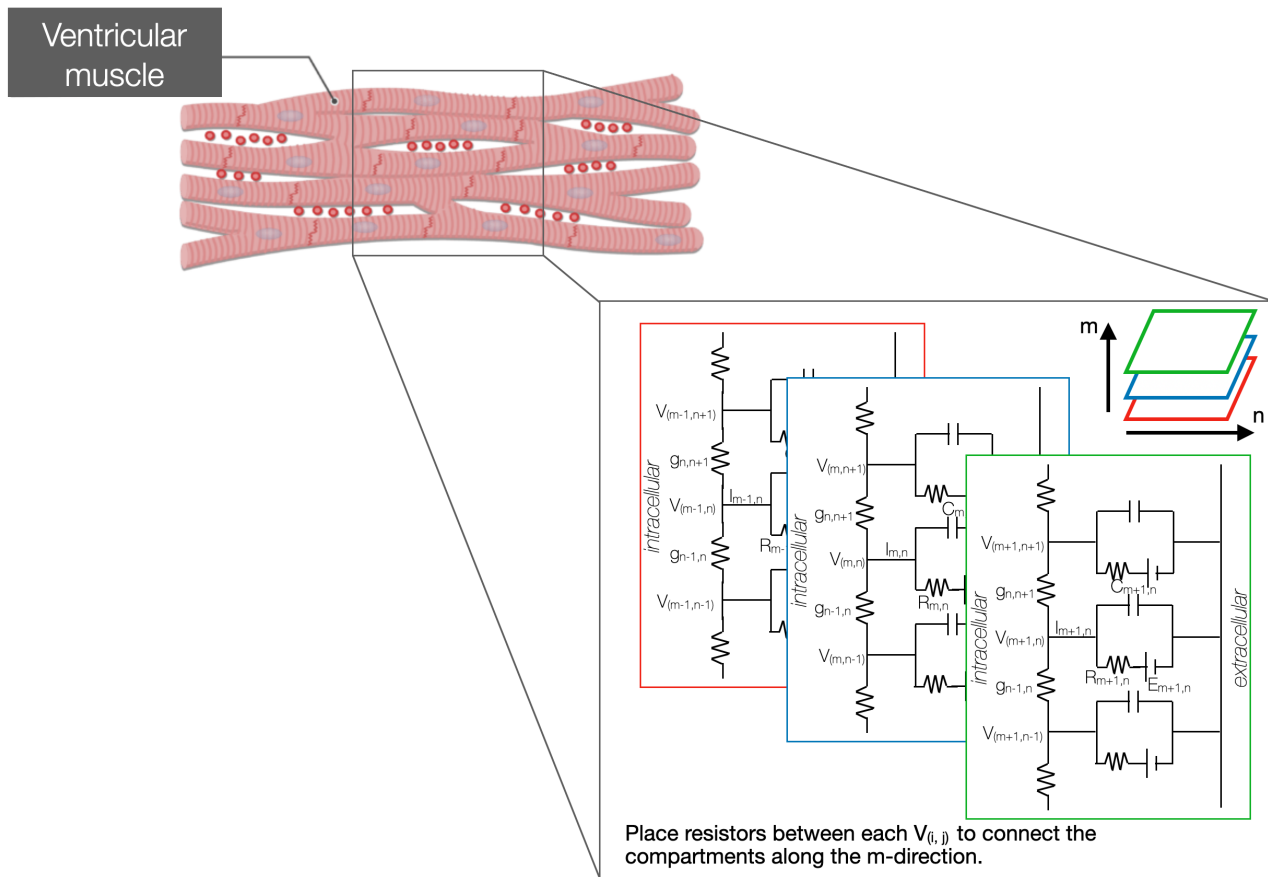


Figure 3: 2D Compartmental model of cardiac tissue.

2.4 Ventricular recordings

Ventricular recordings were obtained using the following procedure:

1. Prepare low-calcium Tyrode solution, 10^{-3} M Tetraethylammonium (TEA) solution, and 20×10^{-6} M Lidocaine solution.
2. Dissect frog heart and submerge in low-calcium Tyrode solution.
3. Closely place two insect pins into the ventricle. Clip alligator clips from the stimulator to the conductive ends.
4. Attach a suction electrode to the ventricle. The suction electrode connects to an audio amplifier that feeds into an oscilloscope that then connects to a analog-to-digital converter for data recording purposes.
5. Set the stimulator such that there is a 2.5 ms pulse duration with a frequency of approximately 1 Hz, and an amplitude of 60 V.
6. Apply light to medium suction from the suction electrode to the ventricle to obtain extracellular recordings of the heart while it is in the low-calcium Tyrode solution.
7. Apply heavy suction from the suction electrodes to the ventricle in the same location to obtain intracellular recordings while the heart is in low-calcium Tyrode solution.
8. Repeat steps 5-7 except perfuse the low-Calcium Tyrode with TEA and wait for 10 minutes before acquiring the recordings.
9. Repeat steps 5-7 except perfuse the TEA solution with the Lidocaine solution.
10. Process the data such that properties such as action potential duration, relative spike amplitude, etc. may be captured and the data may be observed qualitatively as well.

3 Results

3.1 Experimental results

The general amplitudes of the obtained recordings will not be analyzed since each of the recordings, intracellular and extracellular, were not obtained from the same cell or location and therefore cannot be directly compared. Features such as response duration are inspected.

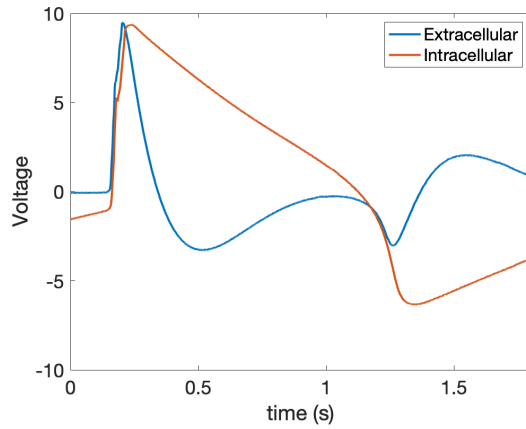


Figure 6: Action potentials captured using extracellular and intracellular recording methods. The frog heart was submerged in low-calcium Tyrode solution.

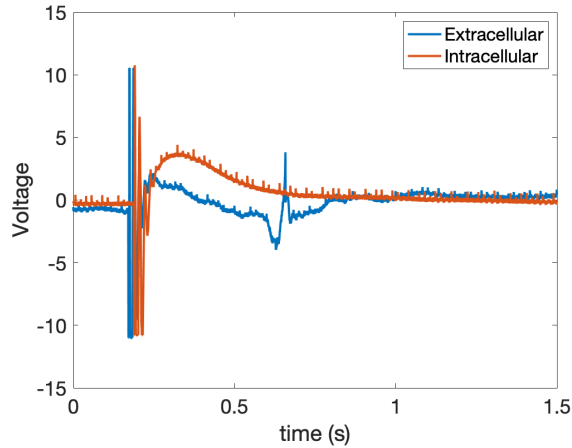


Figure 7: Action potentials captured using extracellular and intracellular recording methods. The frog heart was submerged in 10^{-3} M TEA solution.

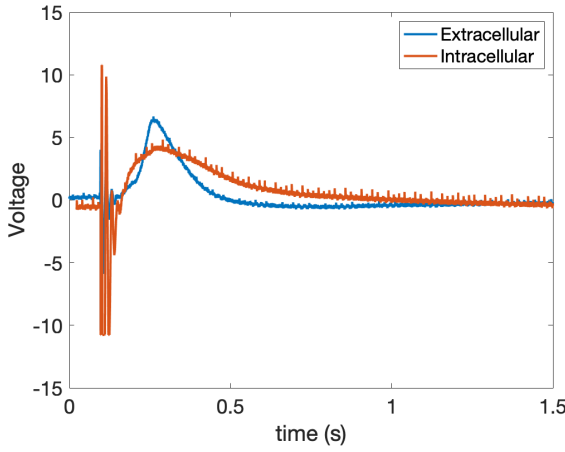


Figure 8: Action potentials captured using extracellular and intracellular recording methods. The frog heart was submerged in 20×10^{-6} M lidocaine solution.

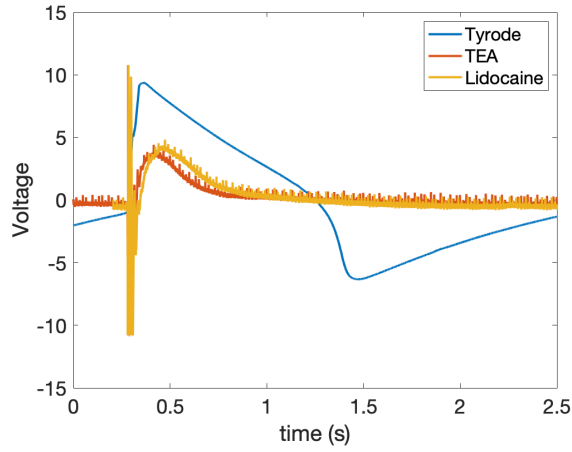


Figure 10: Action potentials captured using the intracellular recording method. The frog heart was submerged in low-calcium Tyrode, 10^{-3} M TEA, and 20×10^{-6} M lidocaine solutions.

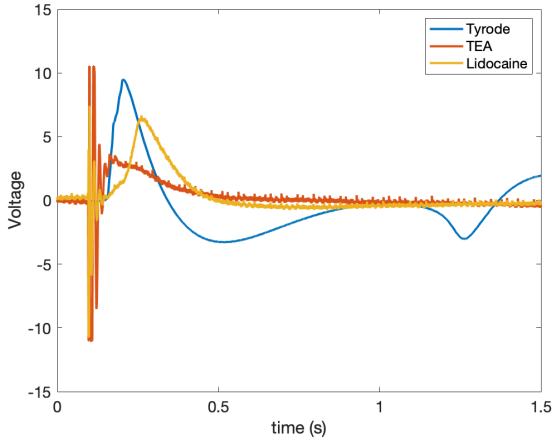


Figure 9: Action potentials captured using the extracellular recording method. The frog heart was submerged in low-calcium Tyrode, 10^{-3} M TEA, and 20×10^{-6} M lidocaine solutions.

3.2 Simulation data comparison

The following simulation results were obtained. A comparison with the experimental, intracellular, low-calcium Tyrode solution was used to select the first set of parameters for the simulation.

Error was calculated after processing the experimental and simulation data. First, the plots were shifted such that the minimum value is zero, then the plots were normalized so that the maximum value is 1. The phases of the captured action potential were aligned and the x-axis is changed to phase, ranging from 0 to 2π . By using this processing method, a direct qualitative comparison can be made. General parameters in the model that were held constant are shown in Table 1.

Table 1: General Parameters

Parameter	Value	Units
Membrane capacitance	1	$\mu\text{F per cm}^2$
Sodium Nernst Potential	50	mV

3.2.1 Intracellular model simulation

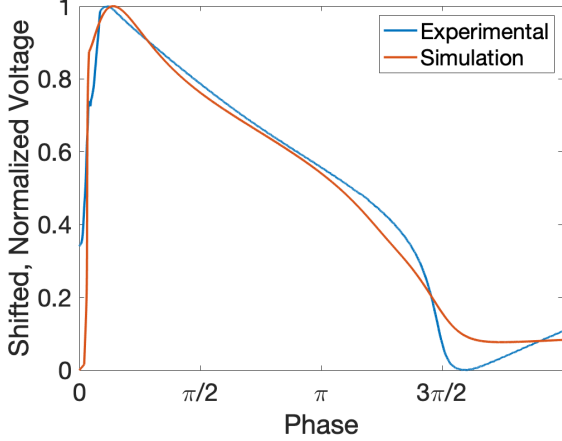


Figure 11: Comparison of the intracellular experimental and simulated action potentials. The frog heart was submerged in low-calcium Tyrode for the experimental measurements. The mean-squared error between the two plots is 0.0041 mV^2 . Parameters values for the simulation are shown in Table 2.

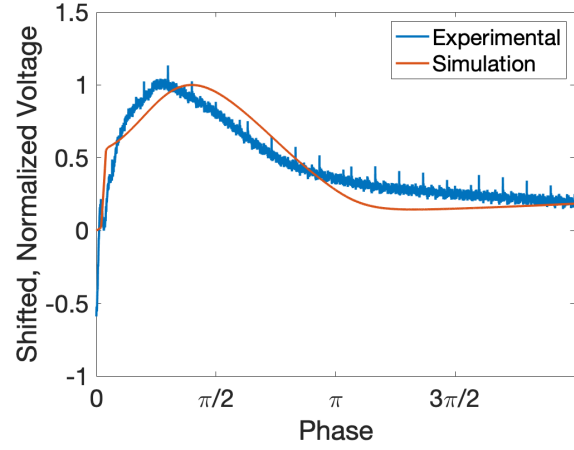


Figure 13: Comparison of the intracellular experimental and simulated action potentials. The frog heart was submerged in $20 \times 10^{-6} \text{ M}$ Lidocaine for the experimental measurements. The mean-squared error between the two plots is 0.0136 mV^2 . Parameters values for the simulation are shown in Table 4.

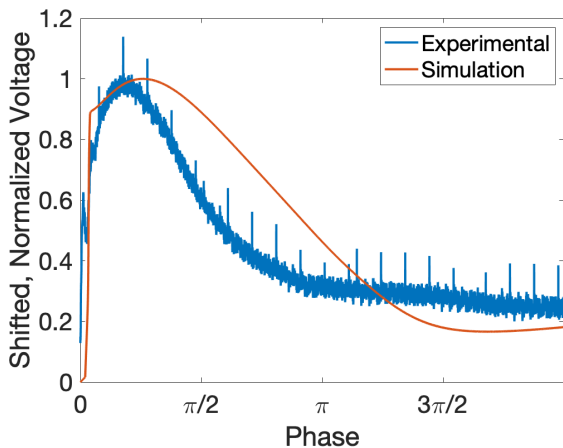


Figure 12: Comparison of the intracellular experimental and simulated action potentials. The frog heart was submerged in 10^{-3} M TEA for the experimental measurements. The mean-squared error between the two plots is 0.0300 mV^2 . Parameters values for the simulation are shown in Table 3.

Table 2: Intracellular Low-Calcium Tyrode AP Parameters

Parameter	Value	Units
Sodium conductance	4	mmho per cm^2
Calcium conductance	0.1	mmho per cm^2
Sodium leakage conductance	0.003	mmho per cm^2
Potassium conductance	1.4	mmho per cm^2

Table 3: Intracellular TEA AP Parameters

Parameter	Value	Units
Sodium conductance	2	mmho per cm^2
Calcium conductance	0.01	mmho per cm^2
Sodium leakage conductance	0.003	mmho per cm^2
Potassium conductance	0.5	mmho per cm^2

Table 4: Intracellular Lidocaine AP Parameters

Parameter	Value	Units
Sodium conductance	0.1	mmho per cm ²
Calcium conductance	0.02	mmho per cm ²
Sodium leakage conductance	0.003	mmho per cm ²
Potassium conductance	1.4	mmho per cm ²

3.2.2 Extracellular model simulation

The extracellular BR-based model produced the plots shown in Figures 14 through 16. For most simulations, the nine-compartment model is used; however, in Figure 14, a simplified single compartment current contributes to the simulated extracellular voltage, specifically compartment number 2 from Figure 4. The compartmental coupling conductance value is 0.02 mmho per cm² for the following extracellular simulations.

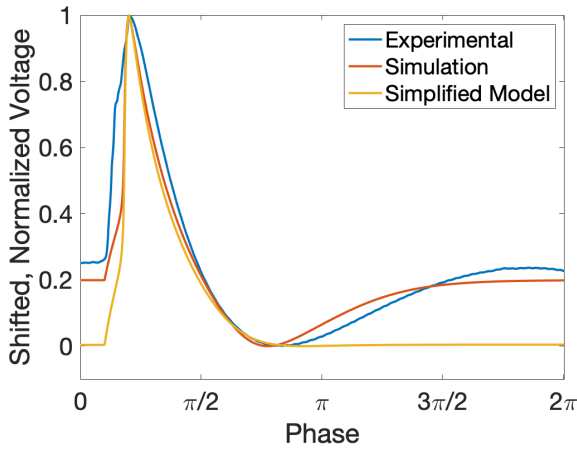


Figure 14: Comparison of the extracellular experimental and simulated action potentials. The frog heart was submerged in low-calcium Tyrode for the experimental measurements. The mean-squared error between the experimental data and the full nine-compartment model simulation plots is 0.0051 mV². The mean-squared error between the experimental data and the simplified, single-compartment model simulation plots is 0.0291 mV². Parameters values for the simulation are shown in Table 5.

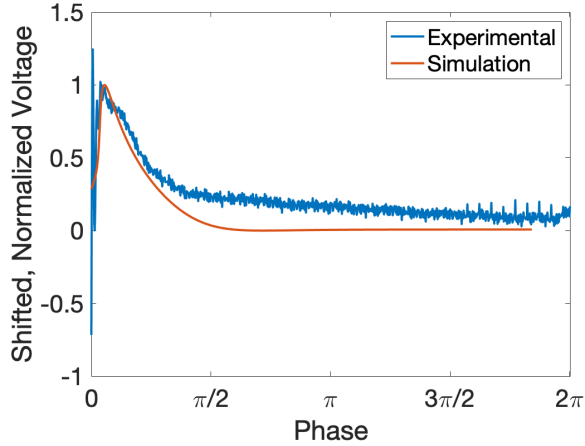


Figure 15: Comparison of the extracellular experimental and simulated action potentials. The frog heart was submerged in 10^{-3} M TEA for the experimental measurements. The mean-squared error between the two plots is 0.0631 mV². Parameters values for the simulation are shown in Table 6.

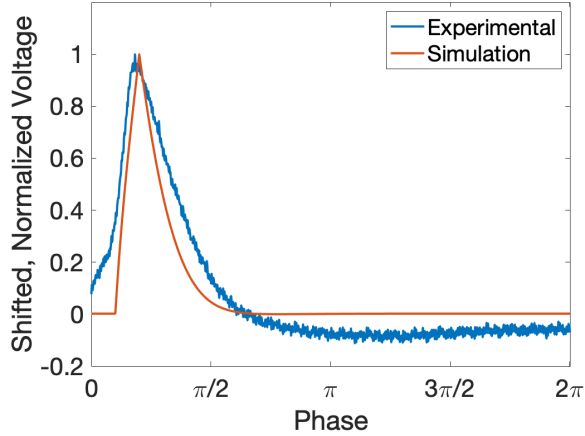


Figure 16: Comparison of the extracellular experimental and simulated action potentials. The frog heart was submerged in 20×10^{-6} M Lidocaine for the experimental measurements. The mean-squared error between the two plots is 0.0116 mV². Parameters values for the simulation are shown in Table 6.

Table 5: Extracellular Low-Calcium Tyrode AP Parameters

Parameter	Value	Units
Sodium conductance	4	mmho per cm ²
Calcium conductance	0.05	mmho per cm ²
Sodium leakage conductance	0.003	mmho per cm ²
Potassium conductance	0.8	mmho per cm ²

Table 6: Extracellular TEA AP Parameters

Parameter	Value	Units
Sodium conductance	2	mmho per cm ²
Calcium conductance	0.01	mmho per cm ²
Sodium leakage conductance	0.003	mmho per cm ²
Potassium conductance	0.001	mmho per cm ²

Table 7: Extracellular Lidocaine AP Parameters

Parameter	Value	Units
Sodium conductance	0.1	mmho per cm ²
Calcium conductance	0.02	mmho per cm ²
Sodium leakage conductance	0.003	mmho per cm ²
Potassium conductance	0.8	mmho per cm ²

4 Discussion

The primary hypothesis is that a qualitative comparison between action potentials measured experimentally can be predicted using a compartmental, BR-based model. Secondly, additions of ion channel blockers in the experimental measurements can be simulated by adjusting ion channel conductance values. Both hypotheses were supported by the results.

The primary hypothesis was supported since the accuracy between the low-calcium experimental and simulated data align with a MSE of 0.0041 mV² for intracellular measurements, and a MSE of 0.0051 mV² for extracellular measurements. Additionally, the secondary hypothesis is supported since the model parameter transitions between low-calcium Tyrode to the TEA and Lidocaine trials are

appropriate based on the known effects of TEA and Lidocaine. TEA is a potassium ion channel blocker and a decrease in the potassium ion channel conductance value in the model caused an improved qualitative match between the experimental and simulated action potentials. Similarly for the Lidocaine, which is a sodium ion channel blocker, a decrease in the sodium ion channel conductance value in the model caused an improved qualitative match between the experimental and simulated action potentials.

Some potential points of error for the results include the inconsistent input voltages that were used to obtain the experimental action potentials. The stimulator output voltage was adjusted to observe action potentials. On a similar note, there is a discontinuity between the experimental data and the simulation data since the voltage values of the experimental data are amplified and the simulation data represent the predicted membrane voltage of the neuron. Additionally, inconsistent recording locations throughout the ventricle were used to observe action potentials. Since the intracellular measurements required a force necessary to burst the neuron, the same cells could not be used to obtain extracellular recordings in the same area. Therefore, comparisons between different cells are made in section 3.1.

Points of improvement are possible for both the experimental setup as well as the modeling work. For future iterations, a battery-powered stimulator would be used to obtain the experimental action potential. Noise is especially prevalent in the TEA and Lidocaine trials and using the battery-powered stimulator may assist in reducing the observed noise. For the model, the parameter values can be better tuned to better align with the experimental data. Optimizers, such as gradient descent or genetic algorithm optimizers, can be used to adjust all the parameters to minimize the MSE between the experimental and simulated results. Additionally, since current is injected at a single compartment of the multi-compartmental model, it is possible that a better fit could be obtained if a different compartment was stimulated or a different number of compartments were used. Having observed that the contribution from the current at the second compartment looked most similar to the experimental data, inferred from Figure 5 a simplification of the model was implemented to observe if a simpler model performed similarly to the full, nine-

compartment model, depicted in Figure [14]. Results showed that the phases of the action potential aligned between the experimental data, the nine-compartment simulation and the simplified single-compartment simulation plots; however, the MSE increased to 0.0291 mV^2 from 0.0041 mV^2 . This increase in error is caused by the offset of the resting membrane voltage. This offset was caused by a lack of up-sweep phase (similar to the hyperpolarization stage in an action potential) in the single-compartment model simulation. Though the MSE increased by over 600%, for some applications the phase approximation may be sufficient.

5 Conclusion

The developed nine-compartment, BR-based model obtained qualitatively similar curves to simulate action potentials measured extracellularly. The model was validated by manually adjusting ion channel conductance parameters to match with experimental data where K^+ and Na^+ channel blockers were applied. Furthermore, the quasistatic form of Maxwell's equations in a uniform volume conductor are a reasonable approximation to the extracellular dynamics of ventricular heart tissue. This method forms a basis for mapping the intracellular activity of electrically-coupled cells to their aggregate extracellular dynamics.

References

- [1] Denis Noble. From the hodgkin-huxley axon to the virtual heart. *J. Physiol.*, pages 15–22, 2006.
- [2] Go W Beeler and H Reuter. Reconstruction of the action potential of ventricular myocardial fibres. *The Journal of physiology*, 268(1):177–210, 1977.
- [3] Gau^te T Einevoll, Christoph Kayser, Nikos K Logothetis, and Stefano Panzeri. Modelling and analysis of local field potentials for studying the function of cortical circuits. *Nature Reviews Neuroscience*, 14(11):770–785, 2013.
- [4] Ellen F Barrett and John N Barrett. Intracellular recording from vertebrate myelinated axons: mechanism of the depolarizing after potential. *Journal of Physiology*, pages 117–144, 1982.
- [5] James Keener and James Sneyd. *Mathematical physiology: II: Systems physiology*. Springer, 2009.
- [6] Matti Hämäläinen, Riitta Hari, Risto J Ilmoniemi, Jukka Knuutila, and Olli V Lounasmaa. Magnetoencephalography—theory, instrumentation, and applications to noninvasive studies of the working human brain. *Reviews of modern Physics*, 65(2):413, 1993.
- [7] Paul L Nunez, Ramesh Srinivasan, et al. *Electric fields of the brain: the neurophysics of EEG*. Oxford University Press, USA, 2006.
- [8] Henrik Lindén, Espen Hagen, Szymon Leski, Eivind S Norheim, Klas H Pettersen, and Gaute T Einevoll. LFPy: a tool for biophysical simulation of extracellular potentials generated by detailed model neurons. *Frontiers in neuroinformatics*, 7:41, 2014.